remote sensing

Article

Multisensor Satellite Data and Field Studies for Unravelling the Structural Evolution and Gold Metallogeny of the Gerf Ophiolitic Nappe, Eastern Desert, Egypt

Mohamed Abd El-Wahed [1,*], Samir Kamh [1], Mohamed Abu Anbar [1], Basem Zoheir [2,3], Mohamed Hamdy [1], Abdelaziz Abdeldayem [1], El Metwally Lebda [4] and Mohamed Attia [4]

[1] Geology Department, Faculty of Science, Tanta University, Tanta 31527, Egypt
[2] Geology Department, Faculty of Science, Benha University, Benha 13518, Egypt
[3] Institute of Geosciences, University of Kiel, Ludewig-Meyn Str. 10, 24118 Kiel, Germany
[4] Geology Department, Faculty of Science, Kafr El Sheikh University, Kafr El Sheikh 33511, Egypt
* Correspondence: mohamed.abdelwahad@science.tanta.edu.eg; Tel.: +20-1273960983

Abstract: The gold mineralization located in the southern Eastern Desert of Egypt mostly occurs in characteristic geologic and structural settings. The gold-bearing quartz veins and the alteration zones are confined to the ductile shear zones between the highly deformed ophiolitic blocks, sheared metavolcanics, and gabbro-diorite rocks. The present study attempts to integrate multisensor remotely sensed data, structural analysis, and field investigation in unraveling the geologic and structural controls of gold mineralization in the Gabal Gerf area. Multispectral optical sensors of Landsat-8 OLI/TIRS (L8) and Sentinel-2B (S2B) were processed to map the lithologic rock units in the study area. Image processing algorithms including false color composite (FCC), band ratio (BR), principal component analysis (PCA), minimum noise fraction (MNF), and Maximum Likelihood Classifier (MLC) were effective in producing a comprehensive geologic map of the area. The mafic index (MI) = (B13-0.9147) × (B10-1.4366) of ASTER (A) thermal bands and a combined band ratio of S2B and ASTER of (S2B3+A9)/(S2B12+A8) were dramatically successful in discriminating the ophiolitic assemblage, that are considered the favorable lithology for the gold mineralization. Three alteration zones of argillic, phyllic and propylitic were spatially recognized using the mineral indices and constrained energy minimization (CEM) approach to ASTER data. The datasets of ALSO PALSAR and Sentinel-1B were subjected to PCA and filtering to extract the lineaments and their spatial densities in the area. Furthermore, the structural analysis revealed that the area has been subjected to three main phases of deformation; (i) NE-SW convergence and sinistral transpression (D2); (ii) ~E-W far field compressional regime (D3), and (iii) extensional tectonics and terrane exhumation (D4). The gold-bearing quartz veins in several occurrences are controlled by D2 and D3 shear zones that cut heterogeneously deformed serpentinites, sheared metavolcanic rocks and gabbro-diorite intrusions. The information extracted from remotely sensed data, structural interpretation and fieldwork were used to produce a gold mineralization potential zones map which was verified by reference and field observations. The present study demonstrates the remote sensing capabilities for the identification of alteration zones and structural controls of the gold mineralization in highly deformed ophiolitic regions.

Keywords: multispectral satellite data; PALSAR; gold exploration; Gabal Gerf ophiolite nappe; thrust-dominated transpressional; gold-bearing quartz veins

Citation: Abd El-Wahed, M.; Kamh, S.; Abu Anbar, M.; Zoheir, B.; Hamdy, M.; Abdeldayem, A.; Lebda, E.M.; Attia, M. Multisensor Satellite Data and Field Studies for Unravelling the Structural Evolution and Gold Metallogeny of the Gerf Ophiolitic Nappe, Eastern Desert, Egypt. *Remote Sens.* **2023**, *15*, 1974. https://doi.org/10.3390/rs15081974

Academic Editor: Thomas Cudahy

Received: 15 February 2023
Revised: 2 April 2023
Accepted: 5 April 2023
Published: 8 April 2023

1. Introduction

A complete succession of Neoproterozoic basement rocks from the Eastern Desert of Egypt constitutes the northeastern part of the Arabian-Nubian shield (ANS) [1–14]. The origin of these rocks has been attributed to an amalgamation of intra-oceanic arcs that occurred during the peak of the Pan-African Orogeny 630 Ma [15].

The Egyptian Eastern Desert (EED) has been divided into three main tectonic sectors, these are the Northern Eastern Desert (NED), Central Eastern Desert (CED), and Southern Eastern Desert (SED) [16,17]. By focusing on the SED where the study area is located, the SED has similar rock units to the CED which are dominated by gneisses, migmatites, ophiolitic succession, granitoids and island arc assemblages (e.g., volcanogenic metasediments and metavolcanics). On the other hand, the SED has a higher proportion of gneisses [14] than the CED, as well as ophiolitic meta-ultramafites that are exposed tectonically as emplaced nappes. While fold-related faults generally associated with pull-apart basins related to the Najd Fault System predominate in the CED, fold-thrust belts in the SED are first-order kinematics that were later overprinted by regional-scale transpression [13,18–23]. Compared to the CED, the SED appears to represent a deeper amount of exposure and is less impacted by the Najd shearing [24].

The southern sector of the SED, particularly where the study area lies is characterized by numbers of suture zones that are decorated with abundant ophiolites (e.g., Allaqi-Heiani-Onib-Sol Hamed-Yanbu suture and Hamisana shear zone) [11]. Many of the gold deposits are found as gold exposures inside the quartz-mineralized shear zones that occur between and within the Neoproterozoic basement rocks (e.g., ophiolitic sequences, island arc assemblages, Hammamat and Dokhan rocks, and post-orogenic granitoids) [9,13].

Structural studies of these shear zones have attributed the formation of these gold deposits to the compressional or transpressional late-stage events of the EAO. Gold-bearing quartz veins in the granitoid units have been recognized as a predominant source of gold in the Eastern Desert (e.g., Sid, Atalla, Sukari, Umm Rus, and Atud areas). Many authors [9,10,13,19,25,26] indicate that major wrench faults and shear zones mainly controlled the gold distribution in the Eastern Desert. The gold mineralization in the SED (e.g., Um Eleiga, Hutit, Korbiai and El Beida, Um Garayat, Haimur, Marahiq) is confined to sutures and major shear zones (Figure 1a,b).

There are about 30 documented sites of gold quartz carbonate veins in the SED that are found where early and late structures are superimposing [9]. All of these gold occurrences in the SED are associated with either healing microfractures in unusual pyrite and arsenopyrite disseminations or with obvious free-milling gold/electrum inclusions in quartz veins [7,26–29].

The southern Eastern Desert contains a variety of geological and structural contexts for gold-bearing quartz veins and associated alteration zones [8,13]. Among these settings are (Figure 1): (i) the intercalated metavolcanic and volcaniclastic metasediments beneath the listvenized serpentinite, and the brittle-ductile shear zones separating them (e.g., El-Anbat, El-Beida, and Hutit deposits); (ii) The ductile shear zones that control the contact between ophiolitic and island arc units (e.g., Haimur, Seiga, Shashoba, Betam, Um Garayat, El-Foqani and Um El-Tuyor deposits) and (iii) The syn- or late-orogenic granitoid intrusions that were either wrapped around or cut by the steeply dipping crenulated shear zones. (e.g., Romite, Korbiai, Egat and Madari deposits).

Remote sensing data and its modern technologies are used now to distinguish the various lithological units and establish the geological structure connected to huge shear belts, in particular the vast and complex terrains, to produce a detailed structural geologic map. The multisensor satellite imagery can be used to detect the alteration zones which allow to track and identify different minerals (e.g., carbonate, iron oxides minerals and clay minerals). Therefore, remote sensing data are considered to be a helpful and cost-effective exploration technique for finding orogenic gold mineralization in hazardous locations all over the world [8–10].

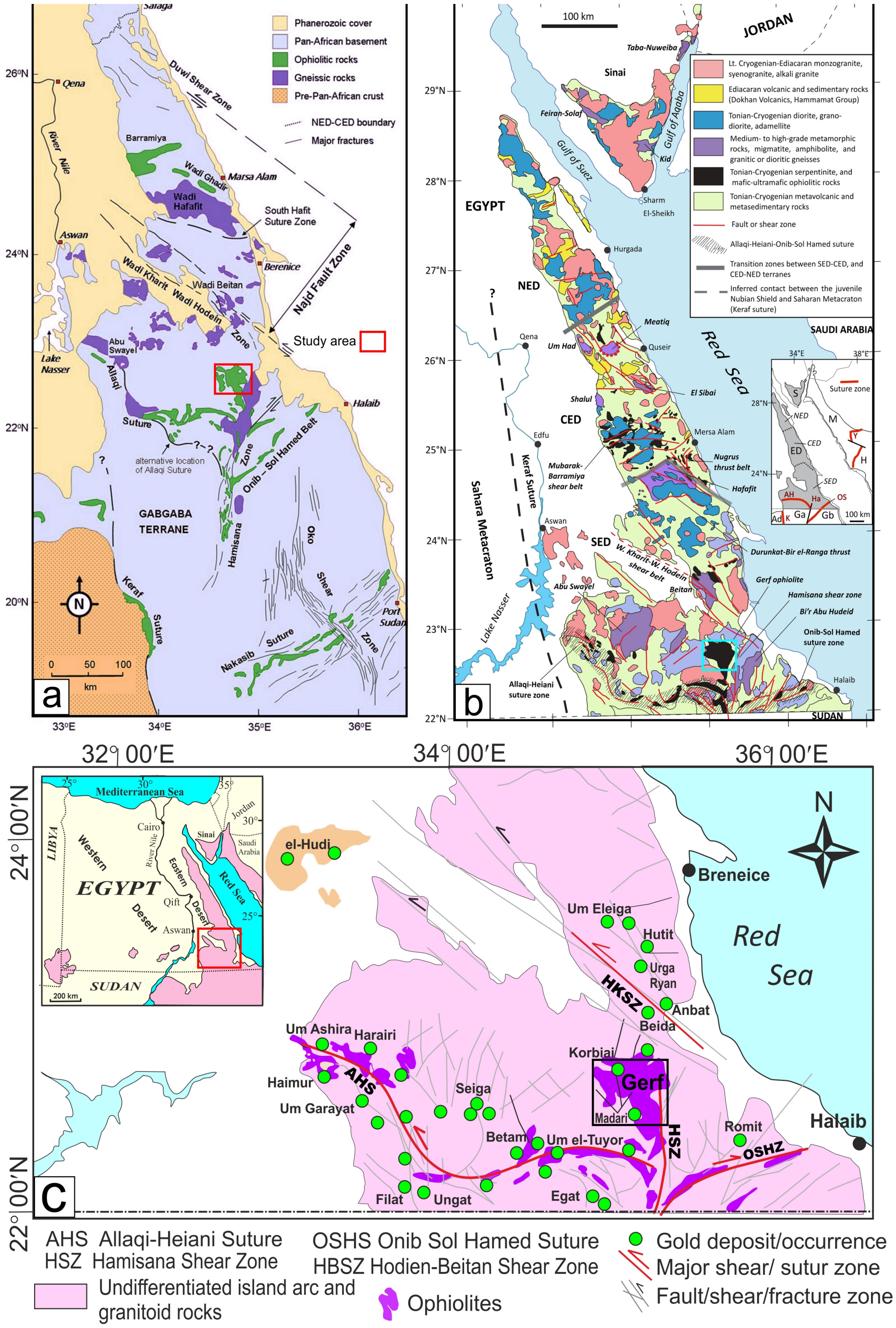

Figure 1. (**a**) The Nubian Shield of northern Sudan and Egypt modified from [9]. The locations of the Gerf ophiolite complex, N–S Hamisana Zone, and Oko Shear Zone are shown. Also shown are the major suture zones, the Allaqi–Heiani, Onib–Sol Hamed, Naskasib and Keraf suture zone of [9]. The extent of the Najd Fault Zone in the CED and SED is also shown, Inset shows a location map of the study area (**b**) Simplified geologic map of the Eastern Desert, Egypt, (**c**) Distribution of the known gold mining sites and gold quartz vein occurrences relative to the major fault/shear structures and ophiolitic masses in the South Eastern Desert terrane modified after [13]. The inset is the map of Egypt showing the location of (**c**).

Utilizing the VNIR and SWIR spectral data, Landsat-8 OLI/TIRS, the Advanced Spaceborne Thermal Emission and Reflection Radiometer (ASTER), and Sentinel-2 data provide efficient remote sensing sensors for differentiating lithological units and alteration zones linked to hydrothermal ore deposits [9,10,13,30–32]. On the other hand, the active microwave remote sensing sensor Synthetic Aperture Radar (SAR) is an effective tool to explore the structural regimes. Wavelengths between 2.0 and 100 cm can be transmitted and detected by SAR, typically at 2.5–3.8 cm (X-band), 4.0–7.5 cm (C-band), and 15.0–30.0 cm (L-band) [33]. In order to map structural features important to orogenic gold mineralization, longer wavelengths (L-band), which are defined by the depth of penetration of radar signals through the Earth's surface, may be helpful [34,35]. Sentinel-1, which has L-band, C-band, and Phased Array type L-band Synthetic Aperture Radar (PALSAR) data, can map the structural lineaments connected to hydrothermal gold mineralization in arid and semi-arid environments [36–38].

The hydrothermal alteration zones can be identified by the diagnostic spectral signatures for OH-bearing, clay, iron oxides, carbonate, and sulfate minerals in the visible, near infrared, and shortwave infrared wave lengths regions [39]. These minerals give certain absorption features in the visible near infrared region (VNIR, 0.4 to 1.1 μm) due to the electronic processes resulting from the transitional elements in the minerals containing Fe^{2+}, Fe^{3+}, Mn, Cr, Co and Ni elements [39]. The hydrous mineral or OH-bearing minerals (Mg-O-H, Al-O-H, Si-O-H) and CO3 acid group have specific absorption features in the shortwave infrared region (SWIR) (2.0–2.50 μm) [40].

In the present study, optical and radar remote sensing sensors data are integrated with the structural analysis and field investigation to reveal the role of structural elements in the distribution and development of the scattered gold–related thrusts, shear zones and quartz veins in the Gerf area.

2. Geology of the Gerf Area

Gerf area (Figure 2) is located at the extremely southern sector of the SED that is composed mainly of a late Neopropterozoic sequence of metamorphic and magmatic assemblages as well as post-tectonic magmatic intrusions. The metamorphic sequence in the Gerf area include both the ophiolitic sequence (e.g., serpentinite, serpentinized peridotite, talc carbonate rocks, pyroxenite, metagabbro and locally pillowed metavolcanics) and the island arc assemblages (e.g., metasediments, schistose metavolcanics). The magmatic assemblage is represented by syn to late tectonic intrusions of gabbro-diorite, granodiorite as well as dykes and veins. The rocks of Gerf area are intruded by Mesozoic alkali-feldspar rocks (e.g., syenite and quartz syenite) [41–44]. In general, the high and low angle thrusts define the contacts between the ophiolitic sequence and the surrounding rocks especially the sheared arc metavolcanics that are overlain by the ophiolitic rocks [45,46].

A sequence of quartzo-feldspathic gneiss striking N-S is juxtaposed and in contact with metasediments (psammopelite-pelites) (Figure 3A) at the southern eastern part of the Gerf area, forming the northern extension of the Hamisana shear zone [47–50]. This sequence is intruded by syn- to late-tectonic granitoids [51,52].

Gerf area contains several prominent mountain peaks such as G. Gerf, G. Korabi, G. Gerf, G. Korab Kansi, G. Direib, G. Madara, and part of G. Abu Hireig (Figure 2). Gerf ophiolite is named after G. Gerf and is regarded as the largest complete ophiolite occurrence in the ANS [41,53,54]. Gerf ophiolite is located to the north of Allaqi– Heiani and Onib-Sol Hamed suture zones and is exposed mainly as a N-S massive lenses and sheet-like bodies of serpentinites (Figure 2). The serpentinite-talc carbonates are regarded as the dominant and largest component of the ophiolitic sequence within the study area, represented by G. Korabi and G. Gerf (Figure 3B) and G. Direib in the central part, by G. Korab Kansi in the western part and by G. Madara and G. Abu Hireig in the southern part of the Gerf area (Figure 2). The serpentinites are mainly of greyish green color (Figure 3B) but reddish green serpentinites (Figure 3C) are also recorded at W. Diqdip. The serpentinized peridotites are coarse-grained bodies enclosed within the serpentinites and cut by calcite-magnesite veinlets (Figure 3D). The contacts between the rocks forming the Gerf ophiolite are marked by a low angle thrust faults. Also, the contacts between the Gerf ophiolite and the island arc assemblages are marked by thrust faults striking N-S, E-W and in some places NW-SE.

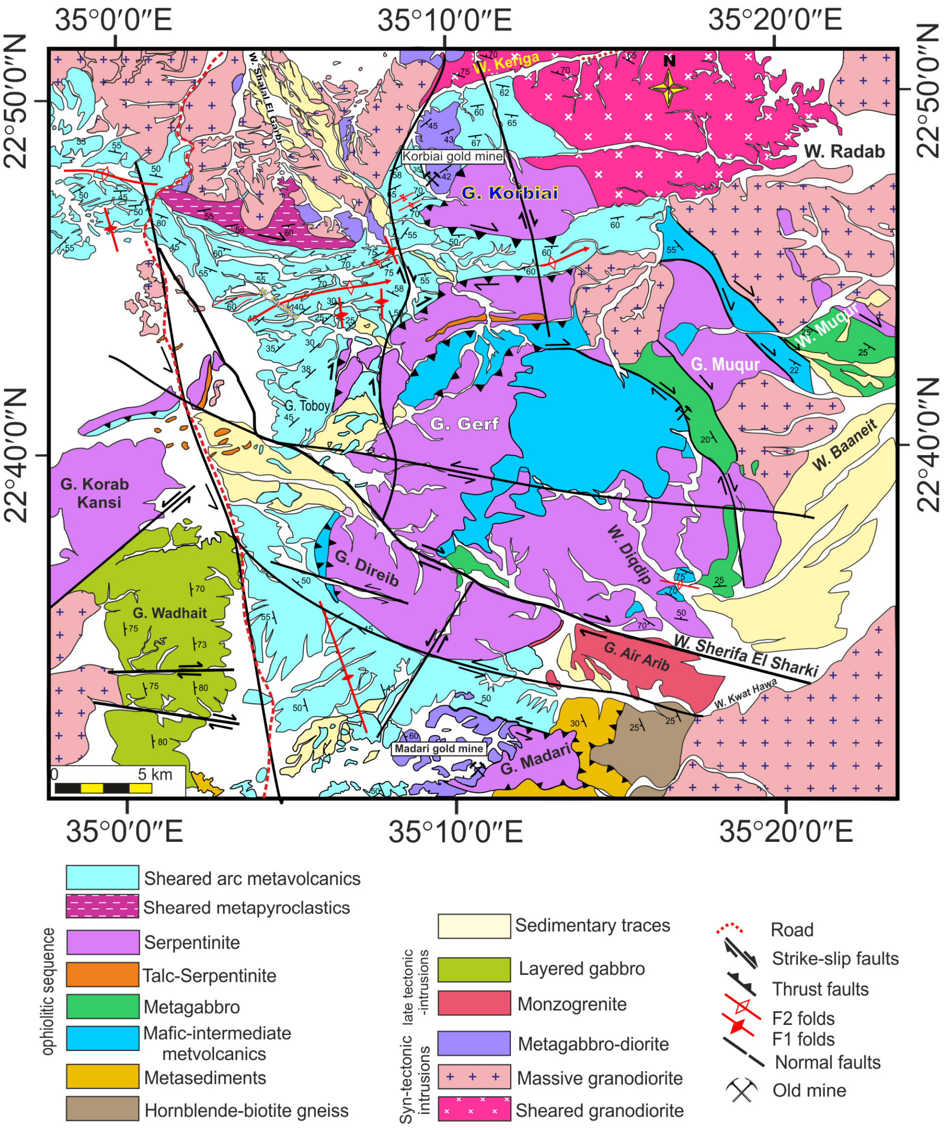

Figure 2. Geological map of the Gerf area based on remote sensing data and field investigations modified after Egyptian Geological Survey and Mining Authority (EGSMA) [44].

The ophiolitic metagabbro (Figure 3E) occurs as small scattered sheared pods distributed only at the eastern and southwestern parts of G. Gerf within the serpentinites. These pods of metagabbros are heterogeneous, sheared locally layered, and form thrust contacts with the surrounding ophiolitic metavolcanics. The ophiolitic metagabbro to the west of G. Muqur has been mined for gold. The ophiolitic metavolcanics are characterized by basic to intermediate composition. They are tectonically emplaced around G. Gerf (Figure 3B). Locally, they are pillowed with a diameter of 10–50 cm [55]. They are exposed as schistose to non-schistose dark color units with aphanitic to vesicular texture.

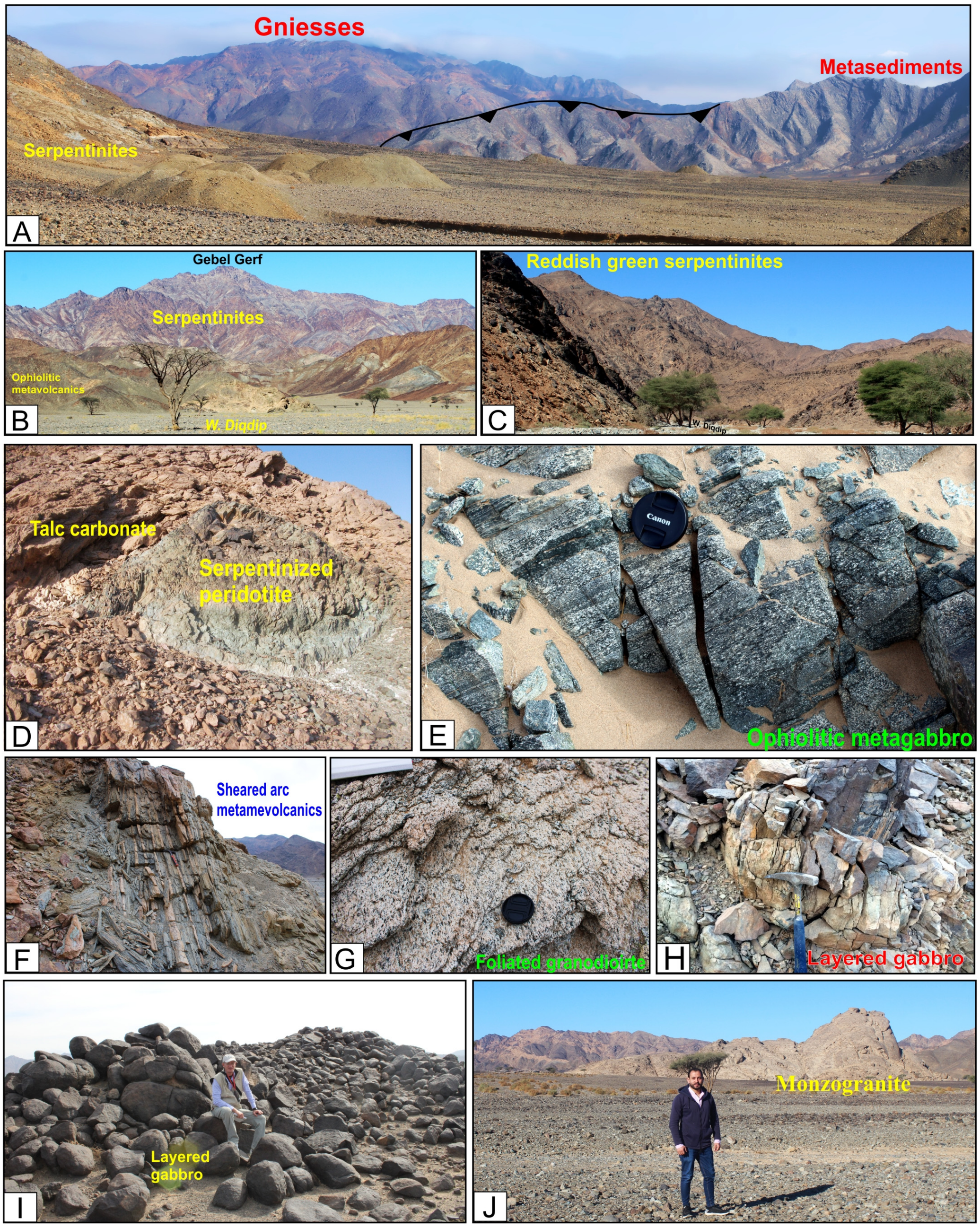

Figure 3. (**A**) A sequence of quartzo-feldspathic gneiss striking N-S juxtaposed with metasediments, (**B**) The greyish green serpentinites of G. Gerf thrust over the ophiolitic metavolcanics (**C**) Reddish green serpentinites along W. Diqdip, (**D**) Small massive masses of the serpentinized peridotite enclosed within the calcite-magnesite rocks of G. Korab Kansi, (**E**) Sheared pod of ophiolitic metagabbro, (**F**) Sheared arc metavolcanics from W. Keriga, (**G**) The foliated granodiorite to the north of G. Korabi, (**H**) The steeply dipping layered gabbro to the south of G. Korab Kansi, (**I**) Layered gabbro to the south of G. Korab Kansi, (**J**) The late-tectonic low relief monzogranites to alkali feldspar granites intrude the serpentinites along W. Sherifa.

The arc metavolcanics are exposed as an E-W striking belt of massive or sheared bodies (Figure 3F) mainly of basic to intermediate composition (e.g., basalt, andesite and basalitic andesite). The arc metavolcanics include some volcaniclastics, agglomerates, and tuffs of calc alkaline affinity [56,57]. They are highly foliated at the western margins of G. Gerf and northeast of the Korbiai gold mine. Moreover, they are transformed into chlorite actinolite schist at the eastern and western parts of the Korbiai ophiolitic mass [57]. The contacts between the Gerf ophiolite and the arc metavolcanics are E-W thrust faults, with the metavolcanics overlain by the serpentinites and talc-carbonate rocks. The arc metasediments are exposed as massive blocks or as schistose thin strips around the serpentinite mass of G. Madara.

The syn-tectonic magmatic intrusions include both gabbro-diorite and granodiorite (Figure 2). The gabbro-diorites occur as intrusive bodies in serpentinites and schistose metavolcanics. The gabbro-diorites are weakly foliated, intruded by granodiorite, and metamorphosed in lower greenschist facies. They gave an age of 729 ± 17 Ma and 736 ± 11 Ma (single zircon Pb–Pb evaporation ages) [58]. The syn-tectonic foliated granodiorites (Figure 3G) are widely distributed and sharply intruded through the whole rock sequence of the Gerf area. To the southeast of G. Korabi, the granodiorites occur as a large high-relief circular body emplaced within the serpentinites and metavolcanics of both ophiolite and island arc. The granodioritic intrusion has been dated to be 551 ± 28 Ma using whole rock Rb/Sr age [47].

Late-tectonic magmatic intrusions have a few exposures and occupy the north and southwestern parts of the Gerf area. They include both layered gabbro and monzogranite intrusions which intruded in the serpentinites, calc alkaline arc metavolcanics, metasediments, and syn-tectonic granodiorite. The late-tectonic layered gabbro (Figure 3H,I) occurs as an NNW-trending belt around G. Korab Kansi, dated 730 ± 6 Ma and 697 ± 5 based on U-pb zircon SHRIMP ages [59] and varies in composition from quartz, norite to olivine gabbro. The late-tectonic layered gabbro intrudes the serpentinite-talc carbonate mass of G. Korab Kansi and the calc-alkaline metavolcanics to the south of G. Direib. To the southeastern margin of G. Gerf, the late-tectonic low relief monzogranites to alkali feldspar granites have a few exposures intruding the serpentinites (Figure 3J) and the quartz feldspathic gneiss. The monzogranites are blocky, undeformed, highly jointed and contain some xenoliths of the older rocks.

A swarm of mafic and felsic dykes of varying trends and widths are intruded in the metamorphosed and magmatic assemblages. There are numerous quartz and pegmatite veins of various trends where gold was historically mined. Post-tectonic syenite intrusions are the youngest rock unit in the Gerf area that sharply intruded the syn-tectonic granodiorite. Petrographically, the Supplementary Figure S1 shows photomicrographs for some selected rock units and alteration zone in the study area.

3. Remotely Sensed Data Characteristics and Analysis

The Landsat-8 OLI/TIRS, ASTER and Sentinel-2B satellite remote sensing datasets were used in the present study for the lithological mapping and mineral exploration. Whereas the Sentinel-1 and ALOS PALSAR datasets were used for mapping the lineaments and major faults/shear zones to deduce their role in the distribution of gold occurrences in the study area. Landsat-8 scene with Path and Row of 173 and 44, respectively, which acquired on 19 April 2021 is obtained as free data from the U.S. Geological Survey. A level 1C of Sentinel-2B (S2B) scenes acquired on 6 July 2022 are also obtained as a free data from the earth explorer website (https://earthexploere.usgs.gov (accessed on 3 September 2022)). In addition, one ASTER scene acquired on the third of May 2015, and named as AST_L1T_00303152004081905 is used in the present study. The three aforementioned datasets were terrain-corrected and cloud-free.

The Sentinel-1 image (S1B_IW_GRDH_1SDV_20210705T154543_2021 0705T154612_027661_034D1E_15CE) was acquired on the fifth of July 2017 and obtained from the European Space Agency (ESA). While two scenes of the ALSO-PALSAR dataset of Fine Beam Dual (FBD) HH + HV polarization (level 1.5, ALPSRP077570440-L1.5 and ALPSRP135480440-L1.5) were acquired from the Earth and Remote Sensing Data Analysis Center (ERSDAC), Japan (http://gds.palsar.ersdac.jspacesystems.or.jp/e/ (accessed on 3 September 2022)). All the remote sensing datasets have been geometrically corrected to the Universal Transverse Mercator (UTM), Zone 36 North projection with the WGS-84 datum.

3.1. *Preprocessing of the Satellite Data*

Landsat-8 contains nine spectral bands, of which seven measure the reflected VNIR and SWIR radiation with spatial resolutions of 30 m for bands 1–7 and 9 and 15 m for panchromatic band 8. Band 9 is useful for cloud detection whereas the ultra-blue band 1 is valued for the coastal and aerosol targets. The multispectral sensor ASTER has a wide spectral range of 14 spectral bands, including three visible and near-infrared radiation bands (VNIR) between 0.52 and 0.86 µm with 15 m spatial resolution, six shortwave infrared radiation bands (SWIR) range between 1.6 and 2.43 µm with 30 m resolution and five thermal infrared radiation bands (TIR) with a range of 8.125 to 11.65 µm and a spatial resolution of 90 m. Sentinel-2B is a multispectral sensor covering 13 spectral bands, including four VNIR bands (0.45 to 0.66 µm), three narrow red edge bands (0.70 to 0.78 µm) and two narrow NIR bands (0.84 to 0.86 µm) as well as two bands in SWIR region (1.6 to 2.20 µm), with a spatial resolution of 10, 20–60 m and large swath width of 290 km [60]. The characteristics of the three optical satellites are presented in Table 1.

Table 1. Summarized characteristics of the Landsat-8 OLI/TIRS, Sentinel-2B and ASTER data [60].

Landsat-8 OLI/TIRS			ASTER			Sentinel-2B		
Band	**Central Wavelength (µm)**	**Spatial Resolution (m)**	**Band**	**Central Wavelength (µm)**	**Spatial Resolution (m)**	**Band**	**Central Wavelength (µm)**	**Spatial Resolution (m)**
1	0.4430	30	1	0.5560	15	1	0.4430	60
2	0.4826		2	0.6610		2	0.4900	10
3	0.5613		3N	0.8070		3	0.5600	
4	0.6546		3B	0.8070	30	4	0.6650	
5	0.8646		4	1.6560		5	0.7050	20
6	1.6090		5	2.1670		6	0.7400	
7	2.2010		6	2.2090		7	0.7830	
8	0.5917	15	7	2.2620		8	0.8420	10
9	1.3730	30	8	2.3360		8A	0.8650	20
10	10.9000	100	9	2.4000	90	9	0.9450	60
11	12.000		10	8.2910		10	1.3750	
-	-	-	11	8.6340		11	1.6100	20
-	-	-	12	9.0750		12	2.1900	
-	-	-	13	10.6570		-	-	-
-	-	-	14	11.3180		-	-	-

Sentinel-1B (S1B) is a C-band synthetic aperture radar (SAR) instrument with spatial resolution ranges from below 5 m to more than 400 km-wide swaths. S1B is composed of single polarization (VV or HH) for the Wave mode and dual polarization (VV + VH or HH + HV) for all other modes of interferometric wide swath (IW) [61,62]. S1B has a spatial resolution of 5–20 m (ESA, 2012), whereas ALOS PALSAR is L-band SAR (1.27 gigahertz) characterized by multi-polarization configuration (HH, HV, VH, and VV), variable nadir angle (9.9–50.8°), and spatial resolution of 100 m with a swath width of 250–350 km for ScanSar mode, 30 m with swath width of 30 km for Polarimetric mode and 10 m with swath width of 70 km for Fine mode [61–64]. The characteristics of the ALOS PALSAR and Sentinel-1B are listed in Supplementary Table S1.

The remote sensing datasets used in the present study have been corrected and processed using different functions of some software packages such as ENVI (Environment for Visualizing Images, v. 5.3), ArcGIS (v. 10.5) (ESRI, Redlands, CA, USA), PCI Geomatica

2016 and Rockworks 16. The atmospheric adjustment has been employed in multispectral data to reduce the effects of atmospheric factors. The Fast Line-of-Sight Atmospheric Analysis of Hypercubes (FLAASH) module attached in ENVI was used to atmospherically correct Landsat 8 and Sentinel-2B. Moreover, the Internal Average Relative Reflection (IARR) was also applied to ASTER data. The Landsat-8 and ASTER data were resampled to 10 m of Sentinel-2 using the Gram-Schmidt spectral pan-sharpening module included in ENVI. The two scenes of the PALSAR imagery are mosaicked and subsetted to the study area boundary. The Enhanced Lee filter was applied to reduce speckles in Sentinel-1 and PALSAR images [65]. The band math in ENVI was used to produce (VV + HV) and (HH + HV) for each of the S1B and PALSAR data, respectively. Then, the PCA was applied on (VV, HV and VV + HV) for S1B data and on (HH, HV, and HH + HV) for PALSAR data to produce PC1, PC2, and PC3 for both radar data. The methodology adopted in the current study is presented in Figure 4.

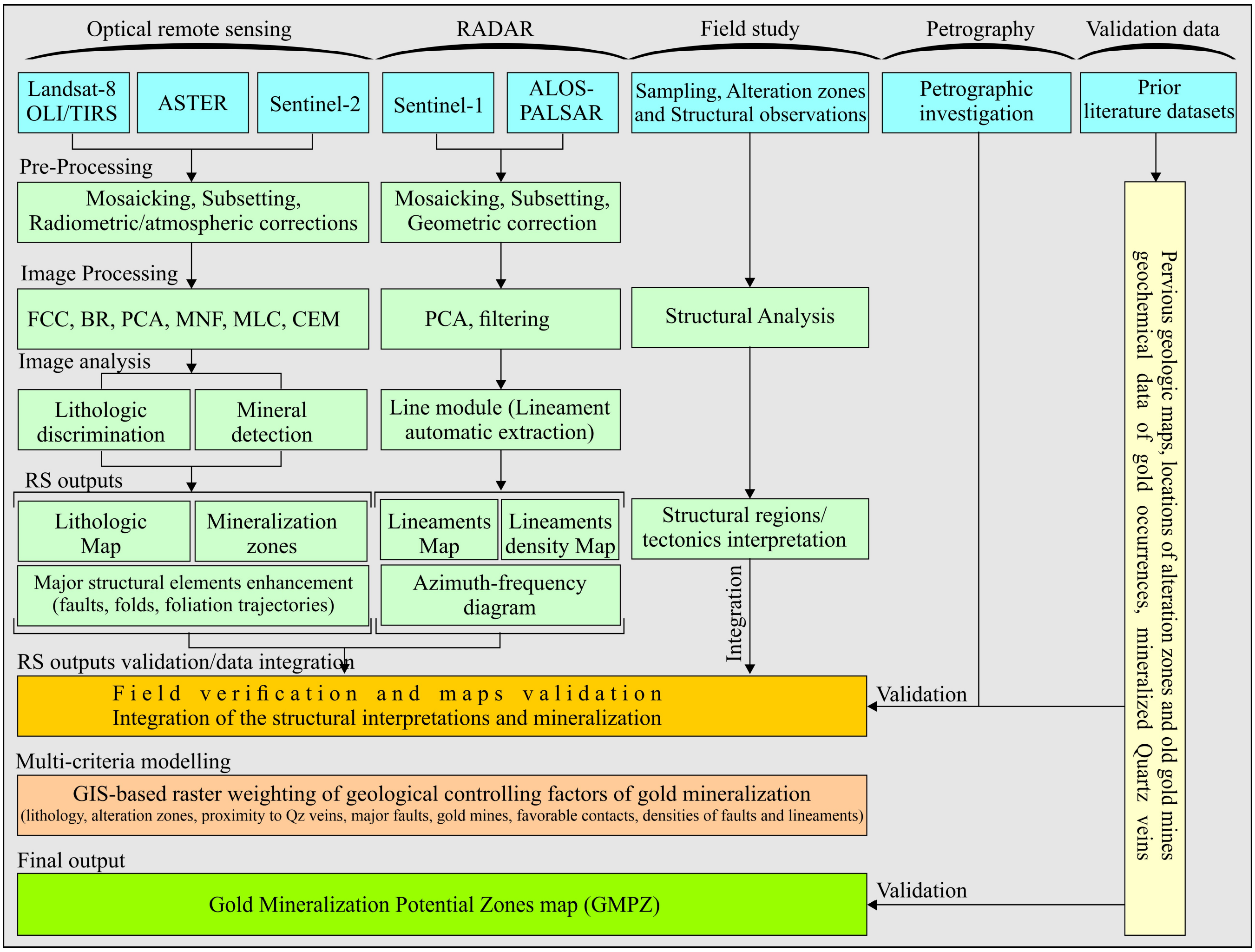

Figure 4. The data and methodology adopted in the present study.

3.2. Processing of the Satellite Data

Variable image processing techniques were used such as false combination color (FCC), band ratio (BR), band math (BM), Principal Component Analysis (PCA), decorrelation stretch, supervised classification and mineralogical indices for lithological discrimination, structural mapping and detection of the hydrothermal alteration zones in the study area. The petrographic study and fieldwork investigation were used to verify the results from the processed satellite datasets.

Ninomiya's mineralogical indices, band ratios of Abrams, Chica–Olma and Kaufmann were also used in lithological mapping and characterization of the iron-oxide, hydroxyl minerals, and clay minerals in the hydrothermal alteration zones. In addition, the PC1 produced from the processed data of S1B and PALSAR were used to extract lineaments in the study area.

3.3. Lithological Mapping Based-Optical Sensors Data

In this study, a group of band combinations (e.g., FCC, BR, PCA, MNF, and MLC) were used for discriminating and mapping the different rock units.

3.3.1. False Color Composite (FCC)

The false color composite is picked out by selecting spectral properties that improve the differentiation of lithological units and hydrothermal alteration zones. FCC significantly facilitates the visual inspection of the produced images and enhances the lithological contacts. In the present work, the selected RGB of FCC combinations is based on Optimum Index factor (OIF) results and prior knowledge of the exposed rock types to ensure the highest level of discrimination. The FCC RGB-753 for landsat-8 and RGB-11 12 8 for S2B were very helpful in differentiating the different rock units (Figure 5A,B), where the ophiolitic rocks and mafic intrusions appeared in dark tones, while metavolcanics, metasediments, granitic intrusions, and gneissic rocks appeared in slightly lighter tones in both combinations. In Figure 5A, the serpentinites and basic-intermediate metavolcanics as ophiolitic units are represented by dark green colors in G. Gerf, G. Korbiai and G. Koran Kansi and brown tones respectively, while ophiolitic metagabbros appears as pale brown color. The arc-metavolcanics have different shades of brown and dark green tones which enhance the foliation trajectories of these rocks. The layered-gabbroic intrusions at the south of G. Korab Kansi exhibit buff pixels. The sheared and foliated granodiorite and gneissic rocks are represented by light to moderate brown tones.

On the other hand, the ophiolitic units appear as dark purple (serpentine) to yellowish green pixels (Ophiolitic metavolcanics) in the FCC RGB-11 12 8 of S2B (Figure 5B). The thrusted contact between serpentinite and ophiolitic metavolcanics is characterized by the creamy light brown pixels of the talc-carbonates and altered rocks. The syn-gabbroic intrusions are represented by purplish green tones, the island arc exhibits dark green to greenish purple tones and granitic bodies and gneisses appear in greenish white to white pixels. The tonal variation in G. Korab Kansi and G. Direib enhances two major NE- and NW- strike-slip faults.

3.3.2. Band Ratio

The band ratio (BR) has been widely used by many authors as an effective method in geological mapping and mineral exploration [13,66]. It is regarded as an effective and maybe the simplest way for improving spectral features since it can draw attention to specific elements that appear to be difficult to emphasize in a single band. The simplest way to do BR is to divide the digital number (DN) values of one band by the corresponding DN values of another band, resulting in a single grayscale image that shows the relative intensities of the two bands [66]. Many earlier investigations have used BR for precise lithological discrimination and qualitative detection of hydrothermal alteration minerals in accordance with the spectrum absorption and reflectance properties of the various rock units and minerals. In the regions rich in the ophiolitic assemblages, Khan et al. [67] used Landsat-7 ETM+ band ratios of 5/7, 4/5, and 3/1 to delineate and map mafic-ultramafic rock units. Pournamdari et al. [68] used the ASTER band ratios of 4/7, 4/5, and 4/1 to outline the ophiolitic assemblages of rock units. Abd El-Wahed et al. [13] performed the Chica–Olma band ratio of 6/7, 6/5, 4/2 and Kaufmann band ratio of 7/5, 5/4, 6/7 of Landsat-8 to map the ophiolite complex and associated rocks as well as the alteration zone mineralization in Wadi Hodein area to the north of the study area.

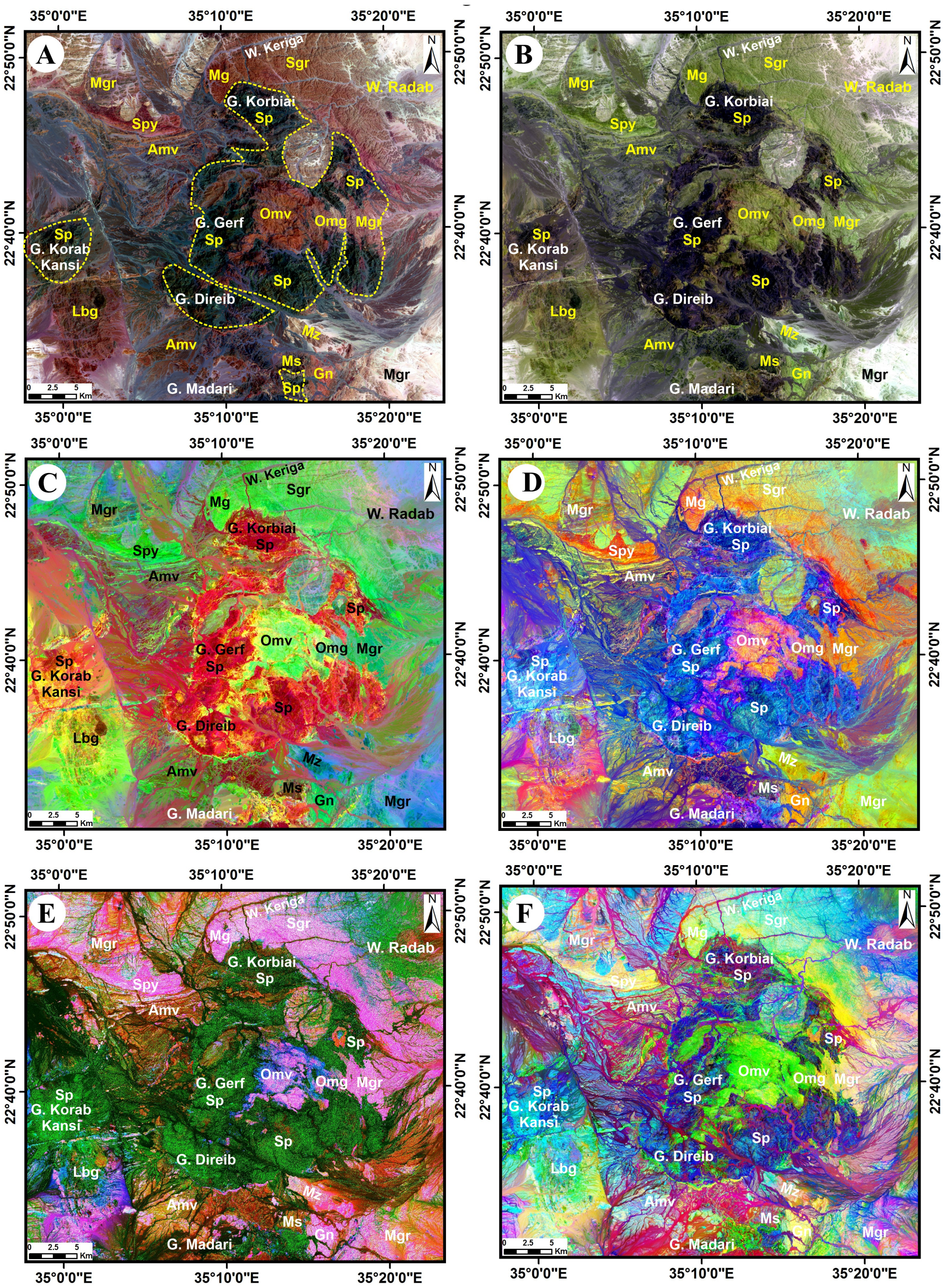

Figure 5. Lithological discrimination (**A**) FCC RGB-753 of landsat-8; (**B**) RGB-11 12 8 of Sentineal-2B; (**C**) band ratio of Chica–Olma (6/7, 6/5, 4/2 in RGB) of Landsat-8; (**D**) band ratio Kaufmann (7/5, 5/4, 6/7 in RGB) of Landsat-8 data; (**E**) Band ratio of 12/11 8/6 12/6 in RGB of Sentinel-2B and (**F**) PCA-432 in RGB for Landsat-8. The yellow dashed line in (**A**) outlined the ophiolite assemblage. Abbreviations: Gn: gneisses, Ms: metasediments, Omv: ophiolitic metavolcanics, Omg: ophiolitic metagabbros, Sp: Serpentine, Spy: sheared metapyroclastics, Amv: arc metavolcanics, Sgr: sheared granodiorite, Mgr: massive granodiorite, Mg: metagabbros, Mz: monzogranite, Lgb: layered gabbros, Wd: wadi deposits.

In that context, the present study adopted the band ratios of Chica–Olma, (6/7, 6/5, 4/2 in RGB) and Kaufmann (7/5, 5/4, 6/7 in RGB) of Landsat-8 data and band ratio of 12/11 8/6 12/6 in RGB of Sentinel-2B data (Figure 5C–E, respectively) which successfully mapped the ophiolitic rock units and associated mineralization. The Chica–Olma ratio 6/7, 6/5, 4/2 image (Figure 5C) clearly demarcated the tectonized ophiolite, in particular the serpentinite units, as a bloody red in G. Gerf to reddish yellow tones in G. Korab Kansi. The ophiolitic metavolcanics are enhanced by the bright yellowish-green pixels whereas the ophiolitic metagabbros exhibit grass green color. The foliated arc metavolcanics are demarcated as dark green to reddish green due to the foliation trajectories, syn-granitic and gneiss as bright light green to greenish cyan, and layered gabbros as greenish yellow tones at the south of G. Korab Kansi. Figure 5C clearly discriminates the altered zones, clay minerals, and talc-carbonate rocks which appear as bright yellow pixels. The altered zones are distributed as bright yellow spotty masses or ribbon-like over the serpentinite or along the sheared contact between the serpentinite and the metavolcanics. Also, in some areas, there is an undulating and/or zigzag contact around the serpentine masses due to the gradual formation of the talc carbonates from the serpentinite metasomatism. Kaufmann ratio 7/5, 5/4, 6/7 in RGB is generated and produced in Figure 5D. The ophiolitic serpentinites highlighted in bright blue colors, ophiolitic metavolcanics exhibit bluish-reddish yellow, arc metavolcanics takes bluish orange and the granitic rocks are enhanced by light orange and yellowish orange shades. The foliated rocks clearly appeared due to the tonal variation of the different rock varieties. The altered zones around the serpentinite masses are diagnostic with a dark purple color. The S2B band ratio of 12/11 8/6 12/6 in RGB (Figure 5E) successfully delineated most of the lithological units and highlighted the sharp contacts between each unit in the study area. The serpentinite is mainly appearing as deep green tones, ophiolitic metavolcanics appear as bluish pink, arc assemblages represented by greenish-brown and layered gabbro appears as bluish green, while syn-late granitic intrusions and gneissic rocks have a light pink signature.

3.3.3. Principal Component Analysis (PCA) and Minimum Noise Fraction (MNF)

The PCA is a common multivariable statistical analysis technique that uses an orthogonal transform to turn a set of correlated variables into a set of linearly uncorrelated variables. This conversion can reduce the dimensions of data without much loss of information [66]. Green et al. [69] proposed the MNF algorithm as a well-known data dimension and noise reduction technique. In this transformation, the data noises are decorrelated and rescaled in the first PCA rotation phase, and the PCs are then obtained from the noise-whitened data in the second. Authors used these linear transforms widely to extract features, noise whitening, and spectral data reduction of remotely sensed data. Due to the greater amount of embedded information, the first PCA and MNF bands were used in the current study for lithological discrimination, hydrothermal alteration mapping, and the detection of key structural elements.

To discriminate the rock units in the study area, PCA and MNF methods were applied to the Landsat-8 and S2B data. Important signatures concerning the occurrence of mineral and rock types that are dominant in the study area can be found in some of the high-order PCs. For the purpose of lithological and mineral identification, several false color RGB composites of the higher-order PCs were utilized. The selection of PCs to perform PCA and MNF composite image were based on the eigenvalues of each Pcs. According to Gupta et al. [70], the enhanced pixels associated with the target mineral or mineral group will appear as bright pixels when the eigenvector of PCs loading is strong (as a positive sign) in the reflection bands of that mineral or mineral group. Conversely, when the loading is negative in the reflection band, the boosted pixels will appear as dark pixels.

Hassan and Sadek [57] used PCA-452 for Landsat-8 and PCA-265 for ASTER data to classify and map the basement rocks in the Gerf area. The PCA-432 in RGB for the Landsat-8 data are produced and shown in Figure 5F. This image successfully delineated the rock units and enhanced the foliated regions. The rock units are characterized by significant colors, where the ophiolitic serpentinite exhibits deep blue to cyan colors, ophiolitic metavolcanics have bright green, and ophiolitic metagabbros take the greenish yellow. The foliated arc metavolcanics have alternative cyan and reddish green tones extended west-east direction and the granitic masses are characterized by fantastic color shades of yellowish green to cyanic in the background of the image.

In addition, the false composite MNF-421 (Figure 6A) and MNF-432 (Figure 6B) have been applied to the satellite data of Landsat-8 and S2B respectively. MNF-421 in the RGB image clearly delineates the ophiolitic assemblage in the center of the image with a sharp contact from the sheared arc metavolcanics and granitic masses. In this composite, the serpentinites masses are outlined and colored obviously by bright green colors, ophiolitic metavolcanics exhibit bright yellow, and ophiolitic metagabbros have cyan colors. The arc metavolcanics are characterized by cyanic green pixels, syn and late-granitic bodies appearing in yellowish cyan to cyan colors with the purple background of the weathered materials. The offset of the NW-strike slip fault at G. Direib can be easily detected due to the shifting of the color variations. The folding in the shared metavolcanics NW G. Gerf can be delineated. The altered zones could also be demarcated by yellow color small ribbons along the periphery of G. Korbiai and thrusted contacts of G. Gerf, and as scattered yellow color masses over the serpentinite rocks at the NW of G. Gerf. The color composite MNF-432 in RGB of S2B imagery (Figure 6B) highlighted the serpentinites by strong cyan color and ophiolitic metavolcanics are represented by dark purple pixels where the ophiolitic metagabbros have bluish cyan color. Whereas the highly deformed arc metavolcanics appear as light cyan to light green tones, foliated arc pyroclastics appear as greenish yellow, syn-granodiorite has dark brownish green to green pixels and layered gabbros have a red color. The alteration zones of iron-oxide, hydroxyl minerals, and clay minerals can be easily detected by reddish-purple pixels around and over the serpentinite masses of G. Korab Kansi, G. Gerf and G. Korbiai.

The three PCA and MNF combinations successfully outlined the sharp thrust contacts between the serpentinites and the various surrounding lithological units, which are thought to be preferable sites for gold mineralization as well as being useful in expediting the foliation trajectories of the highly deformed rocks (e.g., highly foliated arc metavolcanics, meat pyroclastics, and metagabbros).

3.3.4. Ophiolitic Assemblage Mapping

Due to the significant role of the ultramafic-mafic rock units in the gold mineralization process, the present study adopted the mafic index, MI = (B13-0.9147) × (B10-1.4366) and SiO_2 index = 13/12 of ASTER data for the Ninomiya et al. [71] and Ding et al. [72]. The two equations were used to discriminate between the ultramafic-mafic rock units (with high iron, low SiO_2) and intermediate to felsic rock units (with low iron, intermediate to high SiO_2). Moreover, Ge et al. [66] proposed a specialized band ratio combining ASTER and Sentinel-2A data as a band ratio of (Sentinel-2B band 3 + ASTER band 9)/(Sentinel-2B band 12 + ASTER band 8) to distinguish serpentine and ophiolite complex.

The mafic index, MI = (B13-0.9147) × (B10-1.4366) of ASTER data has the power to discriminate clearly the ultramafic-mafic rock units as bright pixels while the intermediate and felsic rock units appear in grey to dark pixels (Figure 6C). The two rock groups are differentiated with a fantastic sharp color contact and the ultramafic-mafic rock units could be easily outlined and mapped (Figure 6D). The thermal bands of ASTER data can determine the SiO_2 index = 13/12. The high SiO_2 content rock units (e.g., gneissic and granitic bodies) appear in bright to light grey tones, but the slightly low SiO_2 content rock units are represented by moderate to dark grey pixels (e.g., serpentinites, metagabbro, basic metavolcanics, and gabbroic intrusions). Ge et al. [66] determined a specific band ratio for mineral mapping and identifying serpentines in the ophiolite assemblage using the spectral characteristics of serpentine minerals as a guide. They introduced a successful band ratio as (Sentinel-2B band 3 + ASTER band 9)/(Sentinel-2B band 12 + ASTER band 8) to discriminate the serpentine and the ophiolite assemblage. Where the Sentinel-2B band 3, Sentinel-2B band 12, ASTER band 8, and ASTER band 9 have the absorption features of serpentine at ASTER band 8 and Sentinel-2B data. Figure 6E represents the grey scale image produced from the application of the band ratio of (S2B3 + A9)/(S2B12 + A8). This band ratio is dramatically successful in discriminating the serpentinite in bright white pixels in the study area. The other rock units in the study area are enhanced by the shades of moderate to dark grey pixels. A pseudo-color version of this image is shown in Figure 6F where the serpentinite is distinguished by a dark blue color surrounded by shades of the orange color of the other rock units.

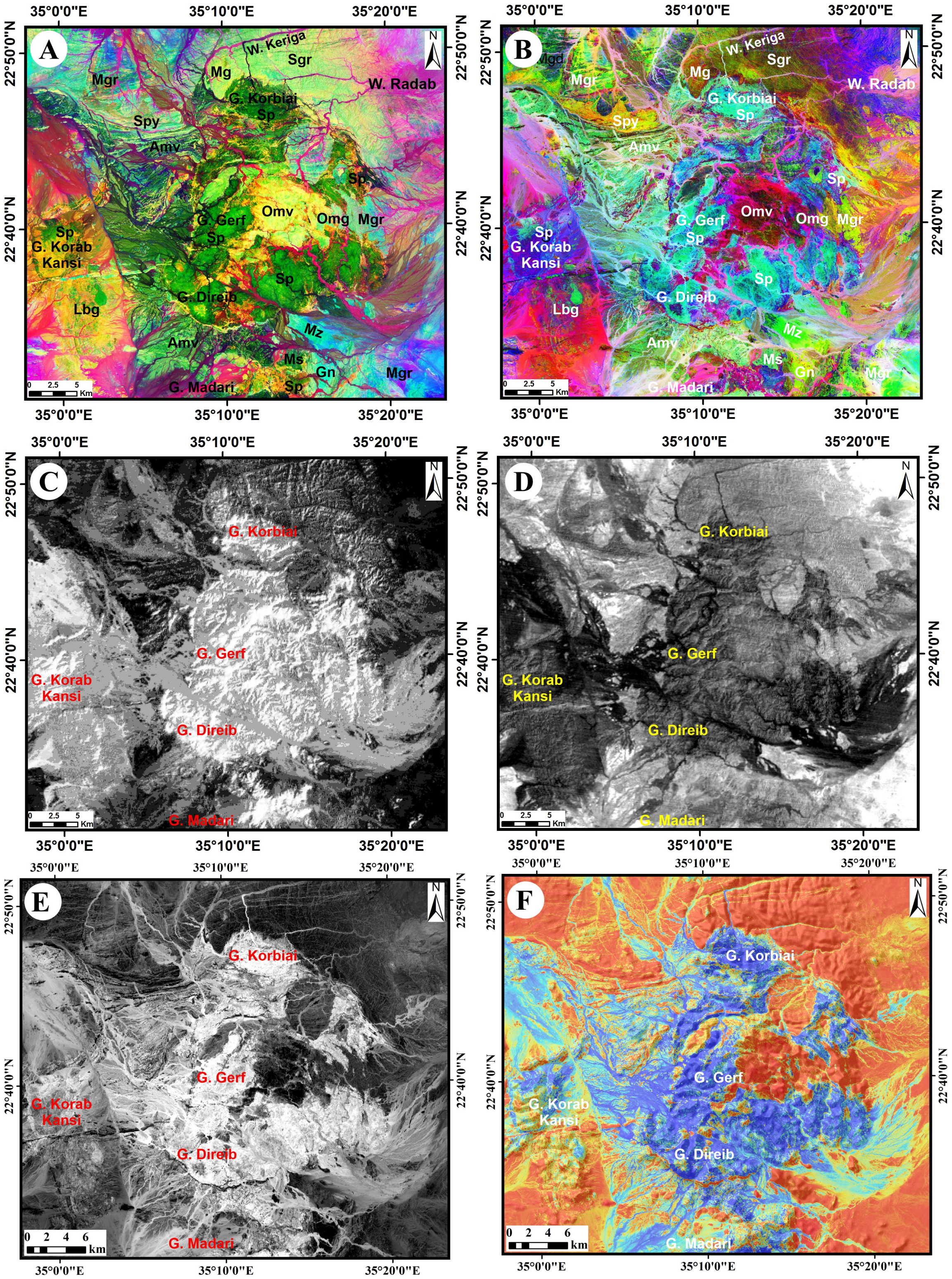

Figure 6. Lithological discrimination; (**A**) MNF-421 in RGB of Landsat-8, (**B**) MNF-432 in RGB of S2B, (**C**) Mafic index, MI = (B13-0.9147) × (B10-1.4366), (**D**) SiO_2 index = 13/12 of ASTER, (**E**) Band ratio of (S2B3 + A9)/(S2B12 + A8), and (**F**) the pseudo-color code of (**E**). For Abbreviations (see Figure 5).

3.3.5. Maximum Likelihood Classifier (MLC)

Digital image classification is considered a powerful method to discriminate and map the different rock units. The choosing of the suitable classifier and using adequate training and testing data are the main factors to give good rock discrimination and produce an accurate classified map. Prior knowledge and the availability of field and previous data can help in improving classification precision. The present study adopted the Maximum Likelihood Algorithm (MLC) to classify the Landsat-8 data. MLC is one of the most prominent supervised algorithms because of its capability to take the size and orientation of the objects into consideration. To build the training classes file, the results of the above-mentioned image processing techniques, the previous geologic maps (at scale 1:250,000 and 1:100,000), and field investigation have been used. The chosen test areas are carefully represented away from lithological boundaries and appropriate to rock unit size. Accordingly, training areas for twelve lithological classes were determined with a satisfactory degree of separability. This training file is used as the base for the MLC classifier to produce a classified image.

Figure 7 shows the final classified geologic map of the study area using Landsat-8 data. The accuracy assessment of the produced map is determined using a stratified random sampling method based on a sample grid representing the locations of rock sample locations and their field attributes. Table 2 shows the confusion matrix which compares pixel by pixel of the classified map and ground truth data with 89.03% overall accuracy and 0.88 Kappa Coefficient. The user accuracies of all classes ranged between 72.83% for the sheared metapyroclastics to 98.68% for the Wadi deposits. Whereas producer accuracies ranged from 61.79% for the arc metavolcanics to 99.29% for the ophiolitic metavolcanics. In accordance with the confusion matrix, the produced ratios are satisfied and reflect the high level of accuracy of the classified process. The arc metavolcanics have the high value of misclassification due to the mixture of signatures with other rock units. This misclassification regards the arc metavolcanics in the study area appeared as small dismembered masses in a vast area of wadi deposits. Moreover, the intercalated felsic and mafic foliated thin ridges can mix the spectral signature with other rock units such as ophiolitic metagabbros and sheared granodiorite. Fortunately, this low value of accuracy of arc metavolcanics does not have a great effect on the overall accuracy of the classified map. The final produced classified map is verified by the testing sample grid, the results of the aforementioned image processing techniques and petrographical investigation. The updated final geologic map is shown in Figure 2.

Table 2. The confusion matrix of the Maximum likelihood method.

		Ground Truth														
	Class	**gn**	**omv**	**omg**	**sp**	**mpy**	**amv**	**sgr**	**mgr**	**mg**	**yg**	**lgb**	**wd**	**Total**	**PA**	**UA**
Classified classes	gn	209	0	1	0	0	4	7	6	0	0	9	0	236	98.58	88.56
	omv	0	704	18	0	0	22	0	0	0	0	0	0	744	99.29	94.62
	omg	0	5	325	0	0	105	0	0	2	0	0	0	437	90.78	74.37
	sp	0	0	0	982	0	12	0	0	0	0	0	57	1051	99.19	93.43
	mpy	2	0	0	0	201	42	11	8	4	0	8	0	276	98.53	72.83
	amv	0	0	0	0	0	773	5	96	8	0	8	105	995	61.79	77.69
	sgr	0	0	0	0	3	103	920	70	0	0	0	1	1097	96.94	83.87
	mgr	1	0	0	0	0	27	1	1731	0	4	0	9	1773	87.91	97.63
	mg	0	0	5	0	0	56	0	0	372	0	5	0	438	95.63	84.93
	yg	0	0	0	0	0	0	0	53	0	381	0	0	434	98.96	87.79
	lgb	0	0	0	8	0	91	5	4	3	0	618	109	838	95.37	73.75
	wd	0	0	9	0	0	16	0	1	0	0	0	1947	1973	87.39	98.68
	Total	212	706	358	990	204	1251	949	1969	389	385	648	2228	10,292		

Overall Accuracy = 89.03% (9163/10292 pixels); Kappa Coefficient = 0.88

For Abbreviations (see Figure 5).

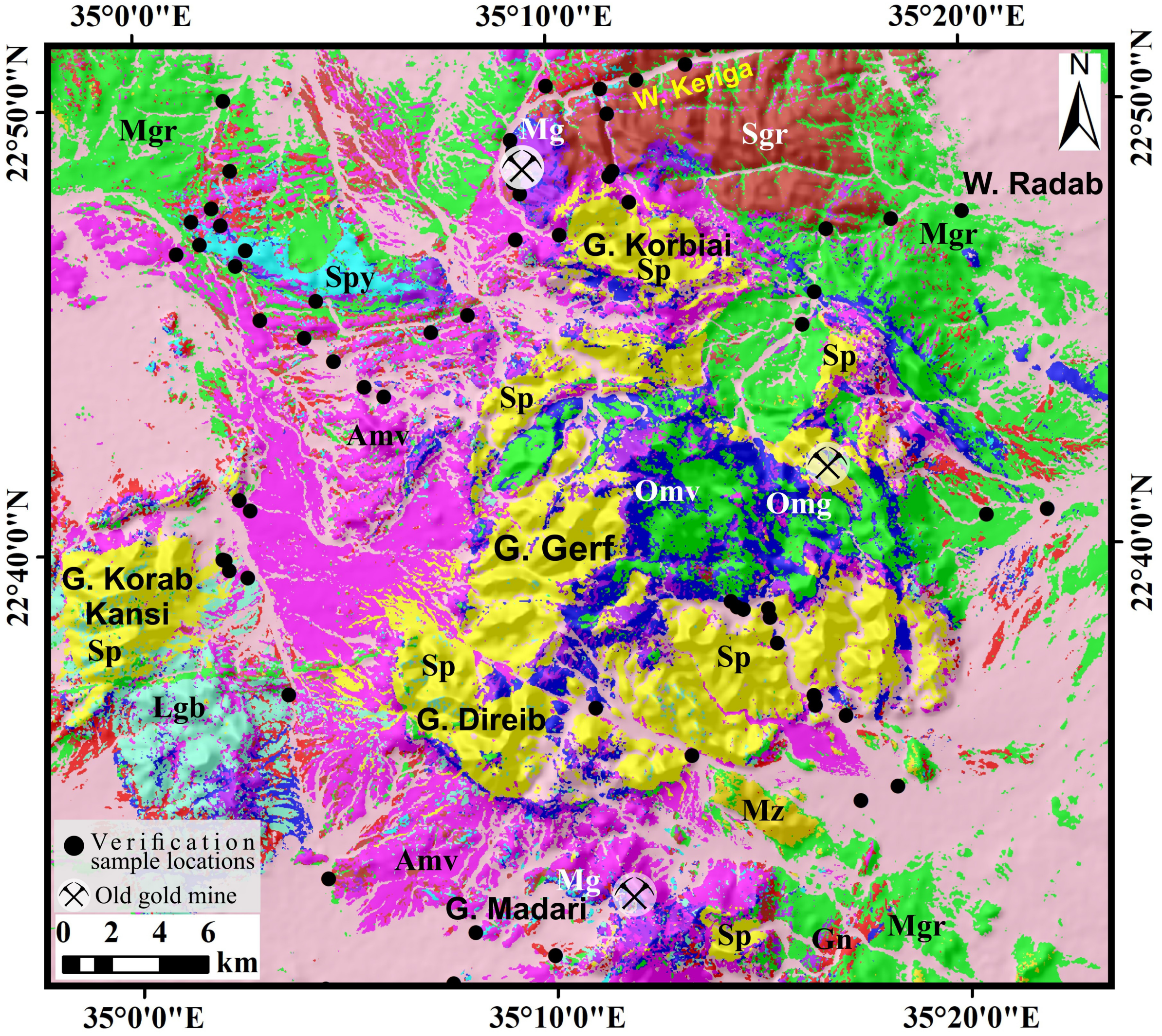

Figure 7. The maximum likelihood classified map based on the Landsat-8 data. For Abbreviations (see Figure 5).

3.4. Alteration Mineral Mapping

3.4.1. Mineral Indices and Band Ratio

Additional BR and mineralogical indicators were used in the current study utilizing ASTER and Landsat-8 data to look for minerals that reflect the presence of specific alteration zones. The spectral ranges of ASTER data are more efficient than Landsat-8 and Sentinel-2B data in detecting the mineral contents in the Earth materials. The hydroxyl minerals and iron oxide/hydroxide zones are found better detected by the ASTER data. Many authors have detected the OH, Fe, Mg-OH-bearing alteration and CO_3 mineral groups, iron oxide/hydroxides and clay minerals using ASTER data (e.g., [13]). Whereas the spectral identification of minerals and rock units can be more precisely determined using ASTER's SWIR channels [56,73]. Bands 11 and 12 of S2B data on the other hand, do not have enough spectral width to distinguish the specific Al-OH, Fe, Mg-OH and CO_3 mineral assemblages. The Landsat 8 images are similar to the S2B images, however, the BRs and PCA of Landsat-8 imagery can be good tools for mineral detections.

The spectral mineralogical indices are defined as reflectance combinations of two or more spectral bands which distinguish the relative abundance of target objects [9,10,13]. Basically, the mineralogical indices of rock-forming minerals are band ratios and mathematical expressions that enable the lithological mapping and detection of hydrothermally mineral alteration zones. According to Ninomiya, [74], the use of mineralogical indices for the ASTER bands can help in identifying lithological and hydrothermal alteration. Therefore, Ninomiya et al. [71] have proposed and used six ASTER-SWIR bands (4, 5, 6, 7, 8, 9) to perform a group of ASTER mineralogical indices to characterize the alteration zones. These mineralogical indices include OH-bearing mineral index (OHI) calculated as (band 7/band 6) × (band 4/band 6); kaolinite index (KLI) calculated as (band 4/band 5) × (band 8/band 6); alunite index (ALI) developed by (band 7/band 5) × (band 7/band 8) and calcite index (CLI) expressed as (band 6/band 8) × (band 9/band 8) (Figure 8A,C–E, respectively).

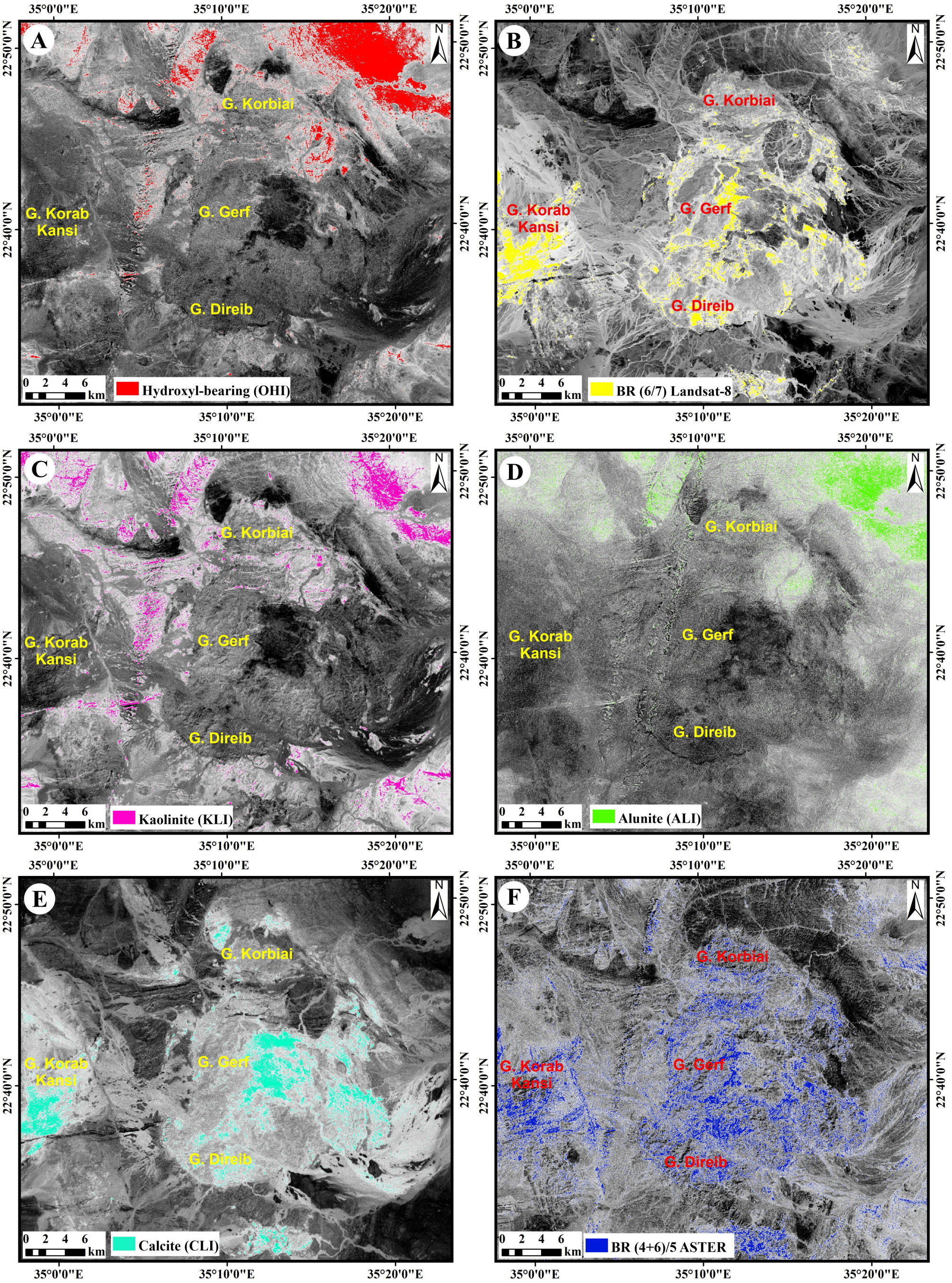

Figure 8. Mineral indices; (**A**) OHI = OH-bearing minerals, (**B**) band ratio 6/7 of Landsat-8, (**C**) Kaolinite index (KLI), (**D**) Alunite index (ALI), (**E**) Calcite index (CLI) and (**F**) Argillic zone using BR = (4 + 6/5) of ASTER.

The gray-scale band ratios images of BR and Ninomiya et al. [71] were thresholded to extract the pixels that represent the target alteration zones/minerals at threshold confidence value 92%. The threshold confidence value was determined as greater than confidence value of 92% by (μ + σ) and confidence value of 95% by (μ + 2σ) where μ and σ represent the mean value and standard deviation values of the resulting band ratio image, respectively. The estimated threshold values of these images are listed in Table 3. The extracted pixels which reflect the spatial distribution of the alteration zones or minerals are superimposed on in their images with a certain color such as red, magenta, green, cyan, . . . etc. (Figure 8A–F). The bright pixels which then coded to the red color show the spatial distribution of OH-bearing altered minerals (Figure 8A). These hydroxyl-bearing minerals are also obtained from BR 6/7 of Landsat-8 (Figure 8B). The distribution of these minerals (Al-OH and Fe, Mg-OH) is superimposed as yellow pixels. As seen in the two figures, the spatial distribution of hydroxyl-bearing minerals is concentrated in granitic plutons, metavolcanics and the contact of serpentine and metagabbros. In G. Koarbiai, G. Gerf, and G. Madari, OH-bearing altered minerals have a spatial agreement with known old gold occurrences.

Table 3. The calculated thresholding which used to detect the target mineral from ASTER data.

Mineral	Min.	Max.	Mean	Stdv	Threshold	Confidence (%)	Area (km^2)
Mineral indices							
OHI	0	255	104	55	215	95	87.1
KLI	0	255	125	62	249	95	55.8
ALI	0	255	130	61	252	95	54.8
CLI	0	255	118	64	247	95	50.9
BR							
Landsat-8 (6/7)	0	255	147	56	203	92	44.8
ASTER (4 + 6/5)	0	255	134	59	252	92	147.4
CEM							
Kaolinite	0	255	132	51	234	95	76.7
Montmorillonite	0	255	93	56	205	95	101.7
Illite	0	255	129	62	254	95	44.1
Talc	0	255	130	61	252	95	49.7
Epidote	0	255	158	58	216	92	58.6
Chlorite	0	255	134	60	254	95	66.9
Calcite	0	255	143	59	202	92	49.8

Stdv: standard deviation.

Advanced argillic and/or Argillic alteration zone is recognized by the existence of kaolinite and alunite minerals. Kaolinite mineral index (KLI) was utilized to extract the kaolinite rich pixels (Figure 8C). Whereas the alunite mineral index (ALI) was performed to detect alunite altered mineral (Figure 8D). The detected kaolinite and alunite have a surface abundance on the contacts of ophiolite assemblage and show concentration on the granitic masses and their drainage and superficial deposits. The propylitic alteration zone is characterized by the existence of calcite that was identified using calcite mineral index (CLI) (Figure 8E). The obvious areas of calcite were indicated as cyan color. The dispersal of calcite is almost concentrated over or around the periphery of serpentinite masses and on the contact between the serpentinite and metavolcanics and metagabbros. The calcite represents the ophio-carbonate rocks that were produced due to the metasomatism of the serpentinite. The areas of the carbonates are confined to the estimated gold contents in G. Gerf and G. Korbiai. The argillic alteration zone in the study area was delineated by applying the ASTER band ratio of (4 + 6/5) (Figure 8F). It is illustrated by blue pixels, which overspread G. Gerf, G. Korbiai, G. Korab Kansi, and G. Madari. The distribution of the gold contents in these areas is matched with the areal distribution of the argillic alteration zone which covers more than 147 km^2 in the study area.

3.4.2. Constrained Energy Minimization (CEM)

The constrained energy minimization (CEM) approach is considered as a spectral mapping technique as proposed by Harsanyi et al. [75]. By suppressing the response of all other features and treating them as the unknown background, it aims to maximize the spectrum response of a target. It depends on the remotely sensed data surface reflectance and the reference spectra of the target alteration zone minerals acquired from the spectral analysis or spectral library. It has become one of the best mineral mapping techniques and most used for minerals abundance mapping [76]. The current study used CEM to distinguish seven alteration minerals which represent three alteration zones of argillic (kaolinite) Phyllic (illite, montmorillonite,) and propylitic (chlorite, epidote, calcite, talc) from the ASTER VNIR-SWIR surface reflectance data. These three alteration zones are favorable zones to the gold mineralization.

The United States Geological Survey (USGS) spectral library (Figure 9) included in the ENVI 5.3 program was used to find the spectral fingerprints of the seven alteration minerals. To fit the ASTER VNIR-SWIR spectral bands' wavelength range, the mineral spectral curves were resampled. The spatial distribution and the surface abundance of the detected alteration minerals are shown in Figure 10A–C. For each reference spectrum, the method generated a band image in grey scale that showed the ideal match pixels in bright to white colors. Each image was thresholded with more than confidence value of 92% to extract the pixels that represent the target alteration mineral and the threshold values are listed in Table 3. Then, the target pixels were superimposed on their images by definite color to enhance the spatial distribution of the interested mineral. Figure 10A shows that the distribution of kaolinite is highly correlated with that extracted from the mineral indices (Figure 8C). In addition, the abundance of the alteration zones defined by ASTER band ratio of (4 + 6/5) (Figure 8E,F) is highly correlated with the surface abundance of two CEM images of phyllic (montmorillonite and illite) and propylitic (chlorite, epidote, calcite and talc) (Figure 10B,C, respectively). It is noticed that the distribution of the alteration zone in the study area (Figure 10D) are confined with the gold mineralization zones documented by El Naggar et al. [77] and El Shimi et al. [78] at G. Gerf area. Moreover, the resulted mineral maps are verified by a well distributed grid of field visits and sample locations of alteration zones in the study area.

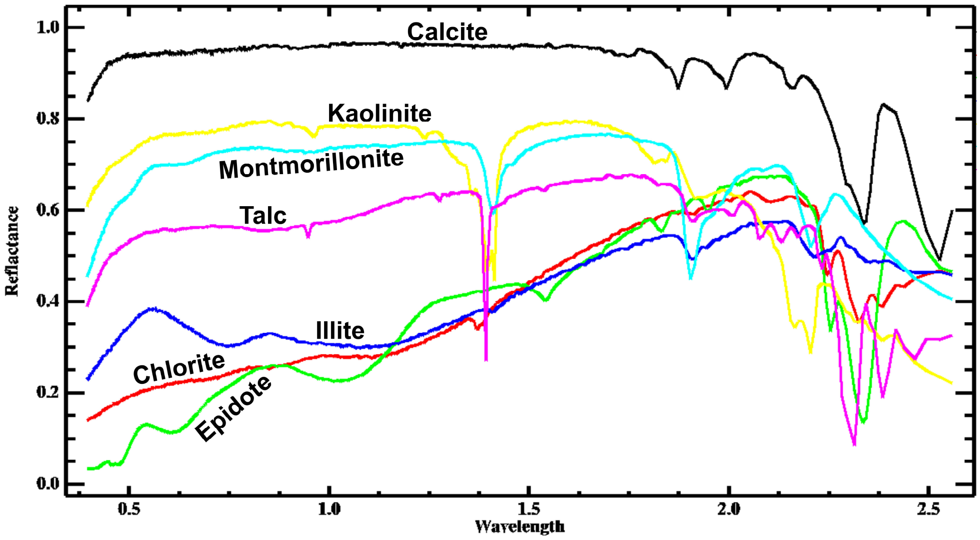

Figure 9. USGS spectral of kaolinite, montmorillonite, illite, chlorite, epidote, calcite and talc.

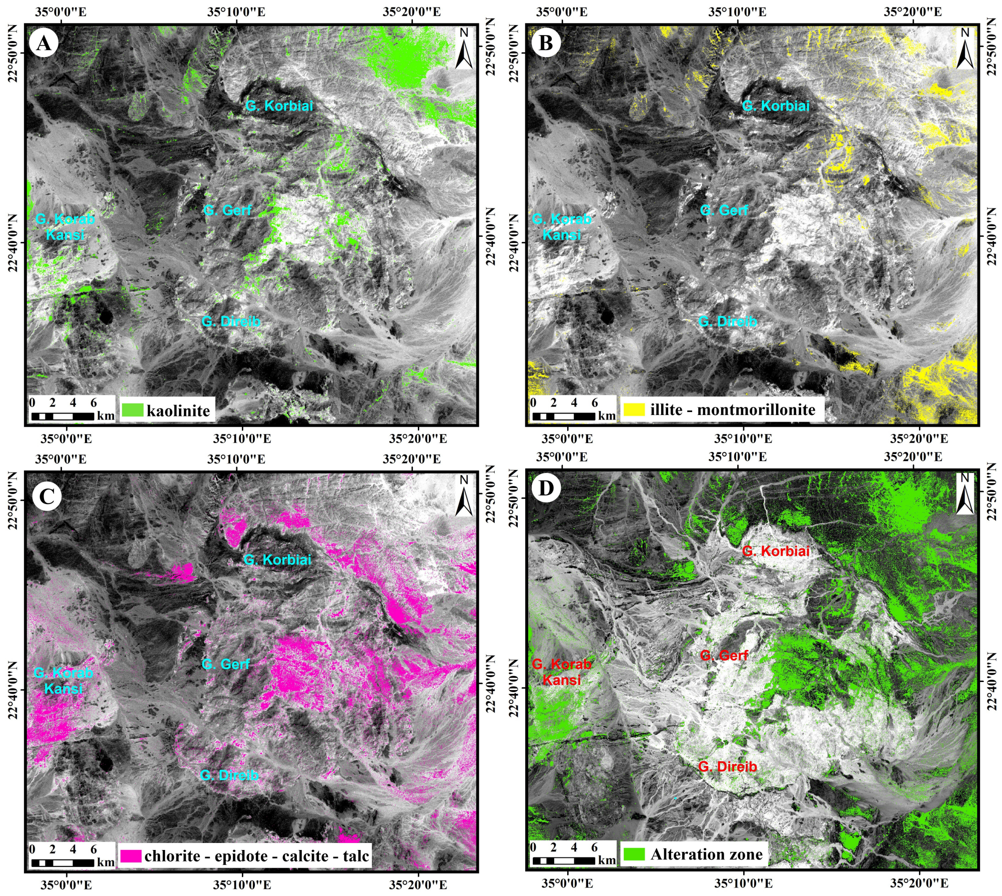

Figure 10. The surface abundance of alteration zones resulted from CEM mineral mapping technique (**A**) argillic (kaolinite), (**B**) phyllic (illite-montmorillonite, (**C**) propylitic (chlorite-epidote-calcite-talc) and (**D**) the grouped alteration zones in the study area.

3.5. PALSAR/Sentinel-1B-Based Lineaments Extraction

Generated backscatter images from the Sentinel-1B (S1B) and high-resolution ALOS PALSAR data with variable off nadir angle and full polarization are required to enhance the structural mapping and lineaments extraction. Geologic mapping and finding the locations of buried minerals or dilatation sites require the quick extraction of lineaments (fault/fracture zones) [79,80], where the hydrothermal ore deposits are located in close proximity to or within these fracture zones. The lineaments/fractures network contributes significantly to the transmission of the hydrothermal solutions and gold mineralization process. In the present study, geometrically reassessed PALSAR and Sentinel-1B images and adaptive enhance Lee filter have been applied to eliminate speckles and enhance structural lineaments [36,81]. The SAR data of both PALASR and S1B were processed and statistically analyzed using the PCA transformation technique to produce the principal components of PC1, PC2 and PC3 images which will aid the identification of the main structural and linear features.

The principal component PC1 extracted from PALSAR and S1B contain the most important information about linear structures in the study area (Figure 11A,B). The two components are subjected to the LINE algorithm function embedded in the PCI Geomatica software to automatically extract the lineaments and linear structures in the study area. The lineaments extraction process is performed using certain values of some parameters as follows; RADI (filter radius) = 10, GTHR (edge gradient threshold) = 50, LTHR (curve length threshold) = 30, FTHR (line fitting threshold) = 3, ATHR (angular difference threshold) = 15, and DTHR (linking distance threshold) = 20. These values are necessary to perform the two steps of the lineaments extraction (edge detection and line-linking) in appropriate level of extraction.

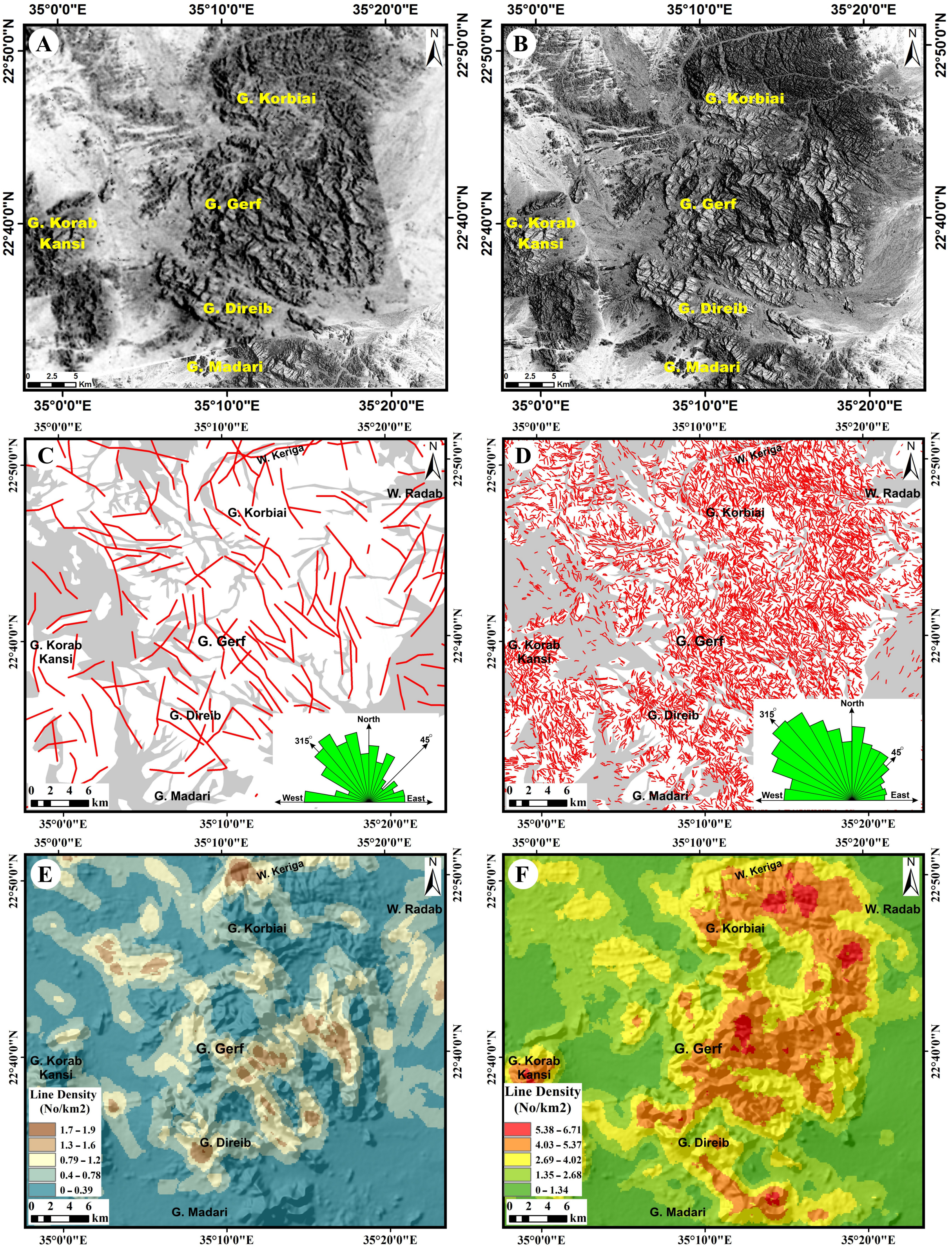

Figure 11. Lineaments extraction (**A**) PC1 of PALSAR, (**B**) PC1 of Sentinel-1B, (**C**) Lineaments map from PALSAR, (**D**) Lineaments map from S1B, and (**E**,**F**) Lineaments density map of PALSAR and S1B, respectively.

The extracted lineaments shapefiles from PALSAR and S1B were exported to ArcGIS 10.5 software to produce the lineaments density maps by means of a line density module. Also, the two shapefiles were exported to Rockworks software 16 to produce the azimuth-frequency diagrams. The two used images of PALSAR and S1B and their associated lineaments density maps and azimuth-frequency diagrams are presented in (Figure 11A–F, respectively) and the basic statistics of the presented lineaments maps are shown in Table 4.

Table 4. Basic statistics of the extracted lineaments from PLASAR and Sentinel-1B.

Parameters/Data Type	PALSAR	Sentinel-1B
Count	533	7425
Minimum (km)	0.03	0.28
Maximum (km)	5.4	2.61
Sum (km)	894.23	4402.04
average	1.68	0.59
Standard Deviation	0.92	0.27

The extracted lineaments maps from PALSAR provide a low number of relatively lengthy linear segments with counts of 533 segments, whereas the extracted lineaments map from S1B reveals 7425 segments which are characterized by high density and short lengths (Figure 11C,D). The two lineament maps show the linear features intensively dissecting all the rock units in the study area with different densities. They show the high densities and linear intersection in the center of the study area overspread G. Gerf. The linear features are confined to the main rock units and decrease in the main streams due to the presence of the wadi deposits and weathered materials. The ophiolitic assemblages and metagabbros exhibit a large number of lineaments that decreases over the arc metavolcanics, granitic and gneissic masses (Figure 11C,D). The total number of the detected lineaments/fractures from PALSAR image is about 533 features with a total length of 894.23 km and a range between 0.03 km and 5.4 km with an average of 1.68 km (Table 4). The total number of the detected lineaments/fractures from S1B image is about 7425 features with the total length of 4402.04 km and their lengths are ranging between 0.28 km to 2.61 km with an average of 0.59 km (Table 4).

The two inset azimuth frequency diagrams show a good similarity in the dominant linear structures directions. They show that the dominant trends of the lineaments/fracturs in the study area are NW-SE, N-S, E-W and NE-SW in decrease order. The total number of the detected lineaments/fractures is about 1281 with the total length of 786.5 km and their lengths are ranging between 0.279 km to 2.56 km with an average of 0.61 km (Table 4). It seems that dominant trends of the lineaments coincide with the major regional faults in the study area. Especially, the two grey scale images (Figure 11A,B) enhance the well-developed foliations of highly deformed arc assemblages, shear cleavages and strike slip faults in the study area. It is clear to notice that a large number of lineaments are parallel to the major strike slip faults of W. Sherifa El Sharki which passes between G. Gerf in the north and G. Dirieb in the south (Figure 11C,D). The two lineaments densities map demonstrate a relatively high matching where the high densities of the lineaments are extend over G. Gerf in the central part of the study area and to the west and north of G. Korbiai in the north of the area (Figure 11E,F). The old gold mining areas are confined to the high-density areas of the lineaments.

4. Structural Setting of the Gerf Area

Structurally, the Gerf area (Figure 12A) is bounded by a major suture and shear zones: (i) E-W Yanbu–Sol Hamed–Gerf–Allaqi–Heiani (YSGAH) –Arc Suture, (ii) syn-accretionary N-S Hamisana shear zone (HSZ) which are located to the southern part of the area and (iii) post-accretionary NW-trending Kharit-Hodien shear zone (KHS) to the northern part of the area. Schematic compilation of the deformational stages in the Gerf area is shown in Table 5, along with comparisons to the Allaqi-Heiani suture [7,9] and Gabel Moqsim area [51] as well as the deformation histories of the East African Orogen [1]. In the Gerf area, the structures pertaining to the early stage of N-S shortening (D1) are not well preserved. The dominant regional foliation (S2) in the Gerf area is striking NNW-SSE to NW-SE (Figures 12B, 13A and 14A–C) and variably deflected by the E-W-striking S3 foliation (Figures 13C and 14D–H). The mylonitic schistosity (S2m) is strongly persevered in gneisses and metasediments in the southern part of the mapped area (Figure 2). S2m strikes N-S to NNE-SSE and it is marked by stretched quartz and feldspar clasts and exhibits preferred orientation at the outcrop scale, gradually develops in the ductile zones. A slickenlines/slip lineation has been recorded as one of penetrative linear structures along the thrust and strike-slip shear zones. The L1 lineation is a stretching mineral lineation, marked by elongated, sometime rotated quartz porphyroclasts in sheared metavolcanics, suggesting also that the deformation was non-coaxial. The L2 lineation is associated to S2 and trends NNW-SSE with an average plunge of 20–40° toward the NNW and SSW. Moreover, the pencil linear structures in the folded and cleaved arc metavolcanics trend N20°W and plunge 25°SSW. During D2, the W-directed thrust planes along the western edge of the Gerf nappe were developed. The D2 thrusts have a characteristic propagation pattern, resulting in imbricate and piggy-back thrust systems. The noticeable thrust-related folds were created by the W- and WSW-propagation of thrusting.

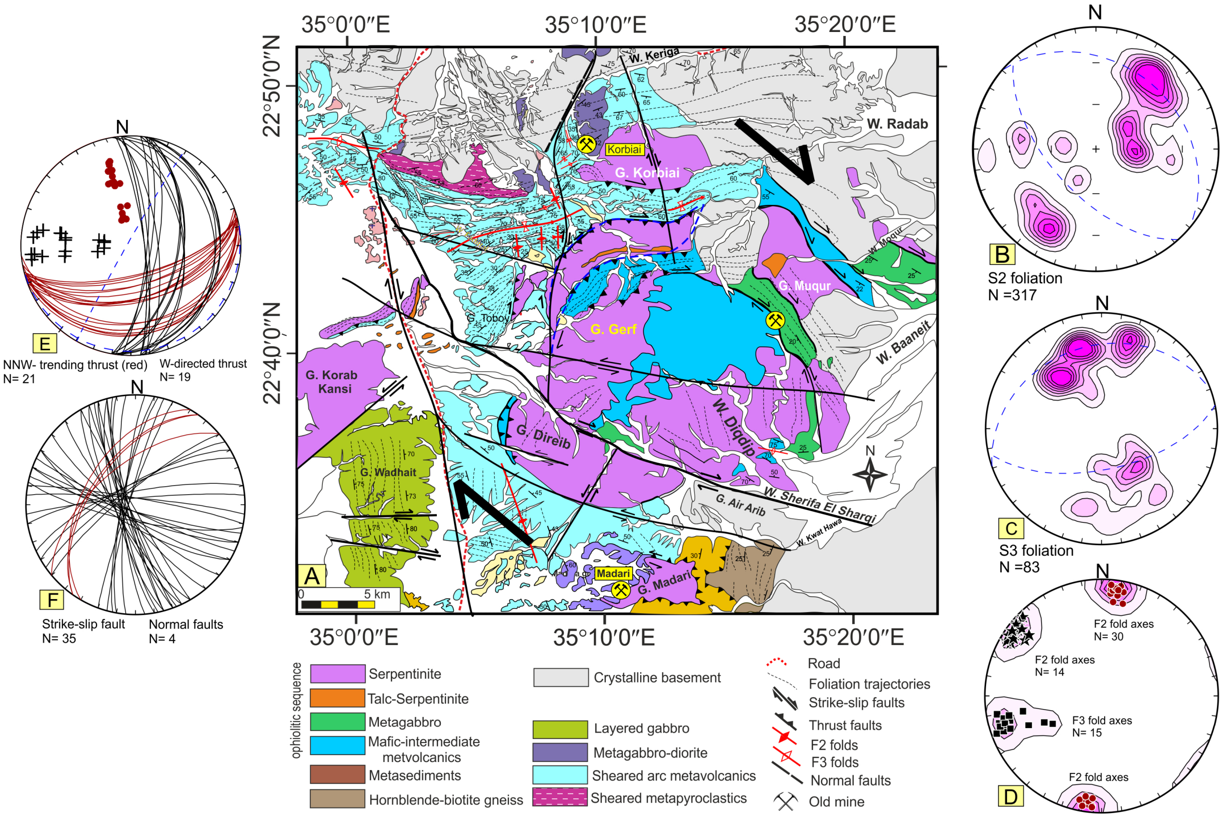

Figure 12. (**A**) Structural map of Gerf area, (**B**,**C**) Contoured stereonet plot of poles to S2 and S3 foliations respectively, contour interval: 0, 2, 4, 6, 8, 10, (**D**) Contoured stereonet plot of trend and plunge to F2 and F3 fold axes respectively, contour interval: 0, 3, 6, 9, 12, 15, (**E**) The red lines are the great circle plots of the NNW-directed thrusts whereas the black lines are the great circle plots of the W-directed thrusts. The black dots are poles to the E-W trending thrusts whereas the red crosses are poles to the N-S striking thrusts, (**F**) The black lines are the great circle plots of the strike slip faults whereas the red lines are the great circle plots of the normal faults.

Table 5. Schematic compilation of the deformational events in the Gerf area along with comparisons to the Allaqi-Heiani suture [7,9] and Gabel Moqsim area [51] as well as the deformation histories of the East African Orogen [1].

	D1	**D2**	**D3**	**D4**
Present study	Missing	ENE-WSW transpression/oblique convergence (Syn-accretionary phase) -Major NNW-striking steeply dipping S1 foliation. -NNE- and NNW-plunging F2 folds. -NNW-SSE thrust-dominated shear zones and thrust segments (W-directed thrusts.	E-W oblique far field compressional regime (post-accretionary phase) -ENE-WSW moderately dipping foliation. -Open ENE-WSW (F3) folds and crenulations overprint the D2 structures. -Formation of S-dipping thrusts. - Formation of NNW-SSE sinistral strike slip faults overprint the early developed NNW-SSE thrust. - Formation of NW-SE dextral strike slip faults	Extensional tectonics and rapid terrane exhumation Brittle deformation brought on by terrane exhumation and cooling after the emplacement of late-orogenic intrusions. -kilometer-scale dextral strike-slip faults strike mainly NW-SE, NNW-SSE, and E-W.
Zoheir et al. [9]	N-S shortening/terrane accretion - Penetrative cleavage foliation (S1), - Mineral stretching lineation (L1), - E- and WNW-oriented folds (F1), - Major E-W to WNW-striking thrust faults.	NE-SW transpression/oblique convergence - Regional NW-plunging folds. - Pervasive NW-SE foliation (S2). - NNW- and NNE-oriented thrusts (T2). - Sinistral transpression along the pre-early developed, regional WNW-oriented thrusts.	E-W compressional regime/N-ward tectonic escape - Major N-striking steeply dipping S3 foliation. - NNE- and NNW-plunging F3 folds. - NNW-SSE thrust-dominated shear zones and thrust segments (T3).	Extension and terrane uplift Brittle deformation, mostly associated with terrane exhumation and cooling subsequent to the emplacement of late-orogenic intrusions. - NNE-SSW and NE-SW strike slip faults
Zoheir et al. [7]	- Moderately NW-dipping thrusts separate the ophiolitic blocks (top) apart from the underlying island arc rocks. - F1 upright and overturned folds with axial traces parallel to the thrust planes (WNW-ESE).	- S2 fabrics. - Asymmetric small-scale and regional NW-SE F2-folds. - L2 lineation plunges mostly to N. - Related extensional shear fractures are subsidiary and mainly confined to the hinge zones of the F2 folds. - Orientation of the major D2 structures at high angles to the major fold-and-thrust structures of D1 reflects a change in direction of the compressional regime during D2.	- Open F3 folds and crenulations overprint the D2 structures - Formation of NNW-SSE strike slip faults extended parallel or subparallel to the axial planes of F3 folds. - The D3 led to general uplift of the central part of the study area. - The D3 is interpreted as a manifestation of a NE-SW non-coaxial compressional stress regime.	- N-trending S4 and NE-trending faults cut the early developed structures. - The D4 records an episode of E-W compression and transcurrent deformation resulting largely in slip reactivation of the pre-existing NNW-trending shear zones, of which, many are gold-bearing.
Zoheir and Klemm [82]	Fold-and-thrust system formation. (Ophiolite emplacement) — Overturned to recumbent folds (F1) commonly verging to S or SE.	NE–SW-compressional regime (Early stage shortening—Right-lateral strike slip faults crosscutting the former fabrics and dislocating the ophiolitic blocks — F2 asymmetric upright folds — Early, penetrative slate foliation (S2) striking roughly NW–SE	E–W-compressional regime (Late stage shortening) — Discrete shear zones, generally NNW-trending, commonly traversing the ophiolitic and island arc rocks — F3 major and minor syncline and anticline structures developed in the ophiolitic and island arc rocks — S3 (NNW–SSE) crenulation cleavage and kinks, coaxial with F3 axial planes.	–WNW–ESE, NNE–SSW and N–S joint/fracture systems traverse the syn- and post-orogenic granites and the pre-existing rocks with no obvious transpression.
Abdelsalam et al. [34]	D1a: N-S shortening produced an imbricate fan with the emplacement of the thrust sheets from north to south. D1b: Continuation of the N-S shortening superimposed as co-axial, but non co-planar deformation in the form of E-trending upright folds which deform the earlier S-verging structure	E-W shortening superimposed on non-axial and non-co-planar deformation in the form of N-trending upright folds and NE-trending sinistral strike–strike-slip faults. which deform the earlier E-trending folds into a crescentic dome interference pattern.	-	-
Kusky and Ramadan [35]	(750–720 Ma) Collision of Gerf and Gabgaba arc terranes: early stages —W-plunging steeply N-dipping axial planar cleavage — E–W striking, steeply N-dipping axial planar cleavage — East plunging isoclinal folds	(750–720 Ma) Collision of Gerf and Gabgaba terranes. late stages — Regional S-vergent thrusts. imbrication of arc/arc accretionary complex	(650–550 Ma) Shortening related to the collision of East and West Gondwana; tectonic escape toward the oceanic free face to N along WNW striking Najd faults WNW–ESE and NW–SE shear zones and open folds, crenulation cleavage, SC fabrics, sigmoidal foliation patterns	(650–550 Ma) NE-striking strike slip faults –E–W fractures
Greiling et al. [52]	Open-tight folds, regional penetrative foliation, metamorphism metamorphic banding, migmatites Island arc andesites and related tufts; generation of an oceanic crust, ophiolitic serpentinites, amphibolites and metagabbro)	Shear fabric, rnylonitic foliation and stretching lineation, regional thrusting and transpression	Regional folds, crenulation and kink bands –E–W fractures	Weak foliation
Stern [1]	Rodinia break-up (late stage) 870–690 Ma Seaf loor spreading, arc and back-arc basin formation, and terrane accretion.	Greater Gondwanaland assembly ~700 Ma Continental collision 750–650 Ma		Greater Gondwana break-up ~550 Ma Crustal shortening. and escape tectonics ~640–550 Ma

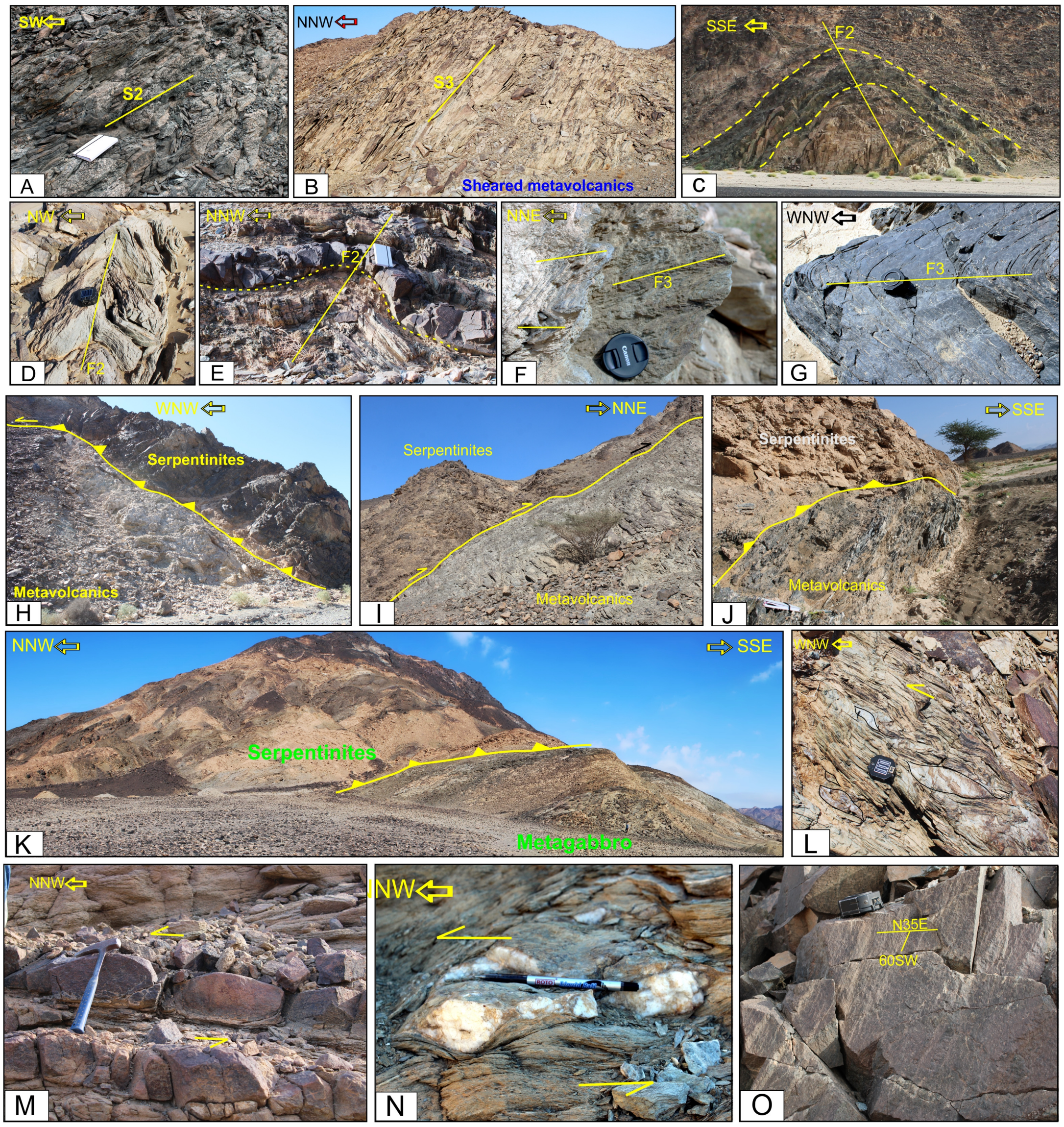

Figure 13. (**A**) S2 schistosity in highly deformed metagabbro along W. Baaneit east of G. Gerf, (**B**) Steeply dipping S3 foliation in sheared arc metavolcanics, northwest G. Gerf, (**C**) Upright open anticline F2 fold with core of serpentinite and limps of sheared arc metavolcanics, north G. Korabi, (**D**) Closure of the F2 fold in foliated arc metavolcanics with fold axis trending mainly NNW-SSE and plunging moderately 15°–35° toward NNW, south of G. Korab Kansi, (**E**) Closure of the open asymmetrical F2 anticline in highly sheared arc metavolcanics with a NNW-trending axis, to the west of G. Gerf, (**F**) Chevron F3 fold in arc metavolcanics at the entrance of W. Daqdib, (**G**) Symmetrical F3 anticlinal fold with a WNW- steeply plunging axis in the basic sheared arc metavolcanic to the northeast of G. Korab Kansi, (**H**) NNW-directed thrust between the serpentinite as hanging wall and sheared metavolcanics to the west of G. Korbiai, (**I**,**J**) W-directed thrust between the serpentinite as hanging wall and sheared carbonatized arc metavolcanics to the northeast of G. Korab Kansi, (**K**) W-directed thrust between serpentinites and metagabbros to the west of G. Madara, (**L**) A series of quartz prophyroclasts in sheared carbonatized arc metavolcanics indicating top-to-W sense of movement along E-directed thrust, west of G. Gerf, (**M**) Boudinaged serpentinite signifying sinistral sense of movement, (**N**) Quartz prophyroclast indicating sinistral sense of movement along NNW-trending strike-slip shear zone, (**O**) NE-striking normal fault with steeply dipping striae toward the northwest.

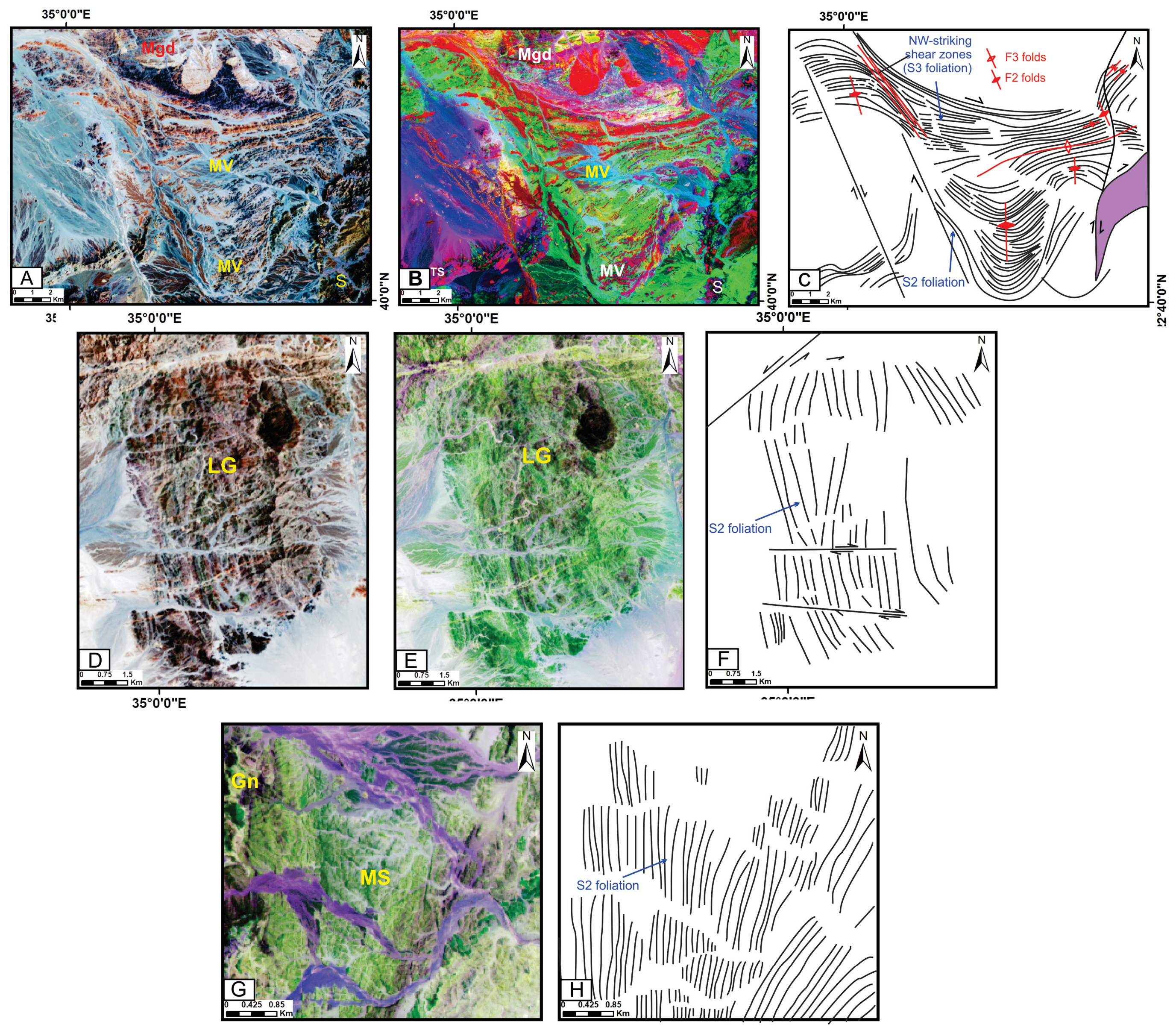

Figure 14. (**A**,**D**) Landsat-8 OLI band composites RGB-753, (**B**,**E**,**G**) Landsat-8 OLI band ratio RGB-7/6, 6/5, 4/2 highlighted the different folding types and trends, and (**C**,**F**,**H**) the resultant interpretation maps of the different fold generations (thin lines for foliation trajectories and red arrows lines are interpreted fold axial traces and major faults (black lines). Gn; gneisses, MS; metasediment, S; serpentinites, MV; metavolcanics, Mgd, sheared granodiorite, LG, layered gabbro.

The northeastern and southwesterly boundaries of the Gerf nappe complex are marked by a conjugate set of sinistral strike-slip shear zones. The movement along these shear zone developed the moderately to steeply dipping mylonitic foliation (S3) that shows a sigmoidal trend inside the strike-slip shear zones and folded into small-scale folds in more constrained and distinct high-strain zones. With the progress of transpressional deformation along sinistral strike-slip shear zones, S2 deflected and rotated from NNW-SSE to ENE-WSW (S3) especially to the north of the Gerf nappe complex (Figure 12A). In mylonite schists, quartz ribbons, feldspar porphyroclasts, and amphibole needles identify down-dip mineral lineation that falls moderately to steeply along planes of intense mylonitic foliation. The L3 mineral lineation that plunges shallowly southwest is only found in steeply dipping strike-slip shear zones.

Two generations of meso and micro folds (F2, F3) with different styles were encountered throughout the study area. Most of these folds have been recorded in the highly foliated arc assemblages (Figures 13C–E and 14A–C). In the sheared metavolcanics, major and minor open to tight symmetrical and asymmetrical F3 folds are common. The fold axes plunge roughly 15° to 35° in both the SW and NE directions (Figure 12E), and the dominant sub-vertical foliation is axially planar to the fold structures. As a result of quartz veins being folded and severely stretched parallel to the main shear plane, boudins and en-echelon structures have developed.

Open to tight recumbent and overturned F2 folds, with their axes trending NNW-SSE and NNE-SSW, and plunge vertically to N, 60°NE, 20°–40°NW. F3 that overprinted and refolded F2 folds are mainly observed in the arc metavolcanics to the north of the Gerf ophiolite nappe (Figures 12E and 13F). The major F3 syncline in the arc metavolcanics along W. Fadittal (Figure 13G) trends N60°–45°E and plunges 18°–30° ENE (Figure 12D). The northern and southern limbs of the F3 folds dip steeply and moderately, respectively (35° to 70° toward NNW and SSE). The steeply dipping limbs of some F3 folds could be attributed to the effect of movement along the NW-trending strike-slip shear zones.

The contacts between the ophiolite slices and the arc metavolcanics are controlled by a set of thrust faults that are oriented from E-W to NE-SW. These thrusts dip gently to moderately between 20° and 50° to the S and SE (Figures 12E and 13H–K). The ophiolitic sequence is a hanging wall between these thrusts and sheared metavolcanics are a footwall. These thrusts show a top-to-N and -NNW sense of movement as revealed by talc carbonate prophyroclasts in the arc metavolcanics (Figure 13L). The S3 foliation and the F3 fold axes run parallel with the strike of the E-W thrusts in the northern and central parts of the area. This suggests that the growth of the F3 folds and the S3 were timed to match the direction of these thrusts. The serpentinite boudins and the quartz prophyroclasts show a sinistral sense of movement along the strike-slip shear zone (Figure 13M,N). On the other hand, a top-to-W sense of movement along the dominant NNW-SSE striking thrusts to the west of the Gerf ophiolite nappe coincided with the development of the S2, L2, and F2 folds. The D3 thrust planes constitute the most prominent structures and they transpose the S2 foliation (or S2m mylonitic foliation of D2) and display S/C fabrics in mylonites. An imbricate thrust system consists of multiple closely spaced thrust faults that are separate between the ophiolitic units themselves, with the ophiolitic metagabbro and pillowed metavolcanics belonging to a footwall and the serpentinites/talc-serpentinites rocks forming the hanging wall (Figure 13H–K).

The most recent generation of fault types is the normal faults that control the contact between the arc metavolcanics and the syn-tectonic granodiorite. The normal faults strike variably between NE-SW (Figures 12F and 13O), NW-SE, and E-W with moderate dip angles between 30° and 50° and a down throw of up to one meter.

Several major strike-slip faults (sinistral and dextral faults) have been inferred from Landsat images and verified during the field investigation with an offset between 500 m to 2 km (Figure 12E). Many of the investigated strike-slip faults have a sinistral shear sense and strike NW-SW. To the south of G. Korab Kansi, the sinistral strike-slip faults strike E-W to NW-SW. A series of minor NW-trending sinistral strike-slip faults have been recorded at the northwestern part of the Gerf area which displaces the arc metavolcanics and syn-tectonic granodiorite.

5. Deformational History

Considering that D1 (N-S shortening) has not been observed in the Gerf area, the following deformation phases are suggested to have occurred there: (i) Syn- tectonic accretionary event (D2); (ii) post-tectonic accretionary event (D3) and (iii) Extension and terrane exhumation (D4). All these deformational events are characterized by brittle-ductile deformation which led to the formation of variable rock fabrics, folds, and faults.

5.1. D2: E-W Shortening Syn-Tectonic Accretionary Event

The Mozambique Ocean was closed during the collision of East and West Gondwana [1] and the development of the D2 compressional syn-tectonic accretionary event, which is represented by the development of N-S trending fabrics and shear zones such as the Hamsiana shear zone (HSZ) to the south of the Gerf area. The southern part of the Gerf area contains well-preserved D2 structures, including S2 and L2 fabrics, as well as F2 folds and N-S striking (W-directed) thrusts (Figure 15A). Moreover, D2 is accompanied by the syn-tectonic magmatic intrusions of gabbro-dioritic and granodioritic rocks which intrude the ophiolitic and arc-assemblages rocks (Figure 15A). Different styles of both the major and minor F2 folds are observed in sheared arc-metavolcanics and ophiolites. The axes of these folds are steeply plunging to N, NNE, and NNW. The D2 thrusts are exposed as W-directed and demonstrate an example of a propagation sequence (Figure 15A). These thrusts occur as an imbricate and piggy-back thrust systems dipping gently to the E and W and were accompanied by refolding of the early F1 folds.

5.2. D3: Post-Tectonic Accretionary Event

D3 is classified as a post-accretionary fault since it formed after the assumed arc-arc collision and was accompanied by transpressive sinistral and dextral movement along the major strike-slip shear zones of the Najd Fault System (NFS) (Figure 15B). In the northern and northeastern parts of the Gerf region, the E-W shortening is considered to have predominated, causing the early thrust faults to reactivate and the refolding of F2 to produce the ENE-trending F3 folds.

In the Gerf area, D3 comprises the development of each S3, L3, F3 and the E-W/ENE–WSW striking thrusts (Figure 15B) as well as the asymmetric β3 boudins of domino's type. The F3 folds are major open to tight anti-formal and syn-formal folds as well as overturned folds with cores and limps consisting of ophiolitic sequence and sheared arc metavolcanics, respectively. The E-W/NE-SW striking thrust faults are characterized by moderately dip angles to S and SE with fault planes decorated by talc-serpentinites and represent NNW-directed imbricate thrusts (Figure 15B) between the ophiolitic units.

The most typical geological features in the Gerf Area are the D3 thrust faults. The serpentinites lenses and the steeply dipping sheets of talc are elongated in the ENE-WSW orientation parallel to the S3 penetrative foliation in the sheared metavolcanics and are developed along thrust planes. Mylonite schists are always used to delineate thrust contacts between the serpentinite slices, the sheared metavolcanics, and other mélange components. The D3 thrusts in the Gerf region exhibit a typical pattern of propagation, where each succeeding thrust grows in the footwall of the preceding thrust in a piggyback thrust pattern (Figure 15A). Moreover, D3 is accompanied by a series of strike-slip faults of sinistral and dextral kinematics as well as the late-magmatic intrusions of layered gabbro and monzogranites. The NW-trending strike-slip shear zones of D3 are marked by dextral/sinistral displacement.

The transpressive character of deformation along the dextral/sinistral strike slip shear zones is shown by the development of thrusts with an opposite sense of movements and the coexistence of strike-slip and compressive structures [83]. This geometry is seen as a huge pop-up (flower) structure connected to the E-W shortening event and sinistral transpressive deformation along the strike-slip shear zones surrounding the Gerf ophiolite nappe (Figure 15B).

The Gerf nappe complex (Figure 15C) was sheared and rotated during a prolonged phase of sinistral shearing (D2–D3) along a series of strike-slip shear zones. During this event, the NNW-striking D2 structures deflected and rotated to the ENE-trending D3 structures synchronously with the development of the S3 mylonitic foliation. The Gerf nappe complex was segmented into several rotated and stretched blocks during sinistral shearing (Figure 15B,C).

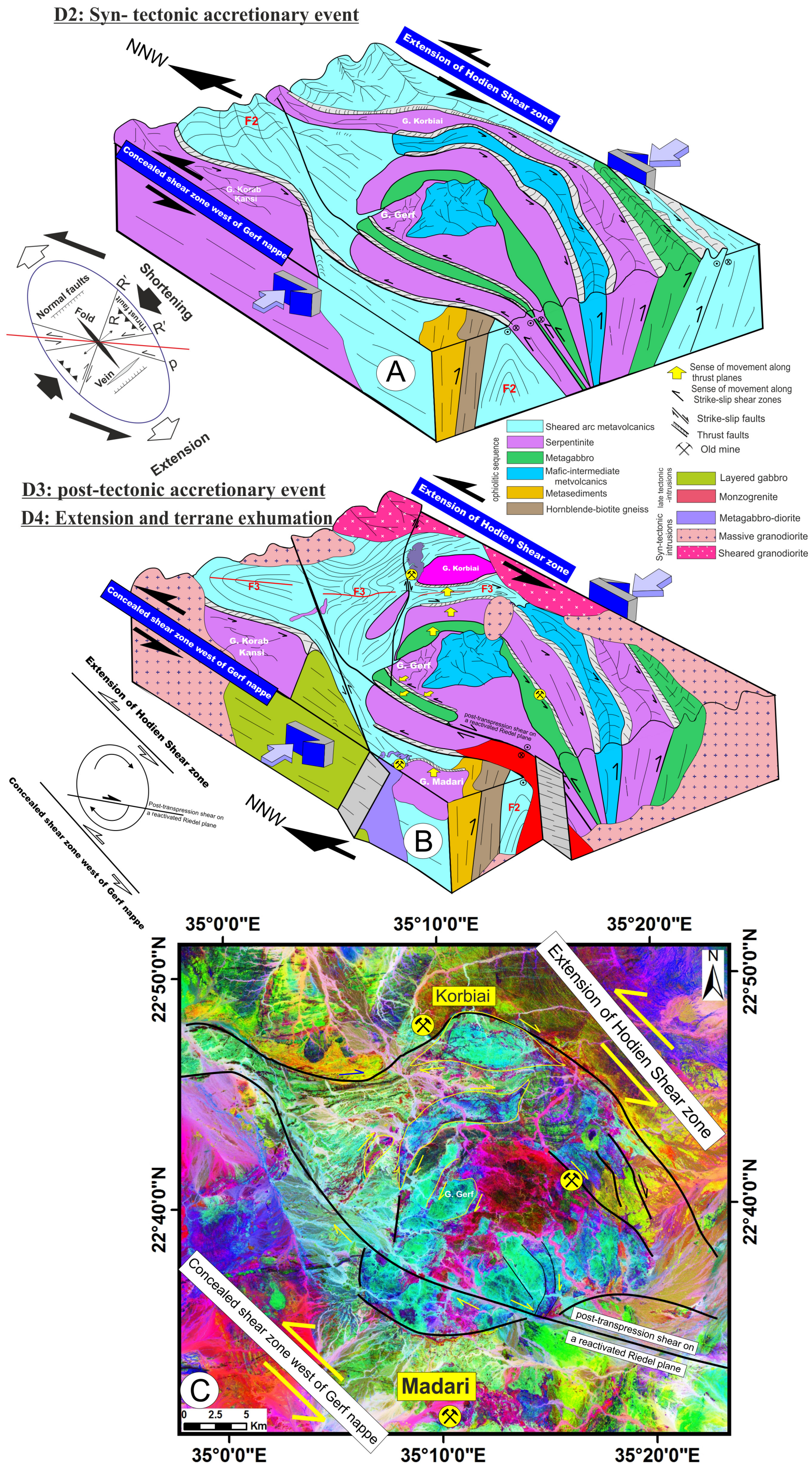

Figure 15. (**A**,**B**) Sketch block diagrams illustrating the structural evolution of the Gerf area, (**C**) MNF-432 in RGB of S2B showing the major Gerf block formed during the sinistral shearing. The yellow circles in C are the old gold mines in the study area.

The late D3 deformational phase features fractures that are either unfilled or filled with injections of quartz and feldspar minerals, which are typical of fluid-assisted deformation and result in quartz veins and veinlets. Asymmetric and symmetric boudins, which are frequently seen in mylonites and ultramylonite, developed in quartz veins. The domino style asymmetric boudins define a sinistral sense of shear. The axes of the symmetric boudins are parallel to the foliation of the mylonitic rocks.

5.3. D4: Extension and Terrane Exhumation

With the intrusion and emplacement of late-orogenic granites as well as terrane exhumation, brittle deformation occurred. The whole rock units, including the post-orogenic granites and the previously developed structures, are displaced by several post-transpression shear zones on a reactivated Riedel plane with a dextral sense of movement. The kilometer-scale dextral strike-slip faults strike mainly NW-SE, NNW-SSE, and E-W (Figures 2 and 15B). Additionally, a significant sinistral strike-slip fault running along the boundary between the layered gabbro and the Korab Kansi serpentinites, striking NE-SW, is present. The NNW-SSE quartz veins developed during D2 and were subsequently deformed by D3–D4 events, while the NE-SW-oriented gold-bearing quartz veins were produced during D3.

6. Gold Occurrence and Shear Zones

The primary source rocks for gold mineralization in the Eastern Desert of Egypt are ophiolites and island arc volcanics as well as granitoids occasionally intruded into or close to the contact of these rocks. The granitic intrusions are accompanied by a convection heated flow system at the contact with the pre-existing metamorphic rocks which leads to the mobilization, leaching, and re-deposition of gold into quartz veins close to this contact [84,85]. Some authors favor the metamorphic origin [86] or the metamorphic-magmatic origin [82] or brittle-ductile shear zones [87] as sources of hydrothermal solutions and spatial distribution of gold deposits.

Zoheir et al. [9,10] traced the gold mineralization back to isolated mesothermal quartz ± carbonate veins that cut through foliated island arc rocks and dismembered ophiolites. Despite the fact that they are typically governed by shear/fault zones, the mineralized quartz veins exhibit a spatial relationship with granitic and gabbroic intrusions that exhibit signs of violent emplacement into the country rocks [9,10]. Basically, the gold deposits in the Gerf area include Korbiai gold occurrence to the north and Madari gold occurrence to the south (Figure 1c).

6.1. Korbiai Gold Occurrence

The old gold occurrences at Beida, Anbat, and Khashab are all located in the Hodein shear zone [13], which also includes the Korbiai gold occurrence to the northwest of G. Korabi. Because of their orogenic character, the mineralized quartz veins in the Korbiai and Madari gold deposits show how they are related to the NNE- and NNW-trending shear zones both spatially and temporally [9]. The isotope data of Korbiai and Romit deposits display overlap with metamorphic or mixed metamorphic and meteoric fluids [7,8,27,28]. In the past, the gold deposits in the Korbiai area were mined or extracted from the gabbro intrusion [57].

The Korbiai gold occurrence area is situated 3 km northwest of Bir Korbiai in an area composed of serpentinites, highly sheared arc metavolcanic rocks, metagabbro-diorite, and granodiorite. The metagabbro-diorite complex consists mainly of metagabbros, quartz diorites, and amphibolites with no sharp contacts between the rock varieties. Particularly at shear zones, the metagabbros are foliated and sheared (Figure 16A). Interstitial quartz is injected throughout the metagabbro rocks. The granodiorite is slightly foliated and forms numerous dissected hills of low to moderate relief.

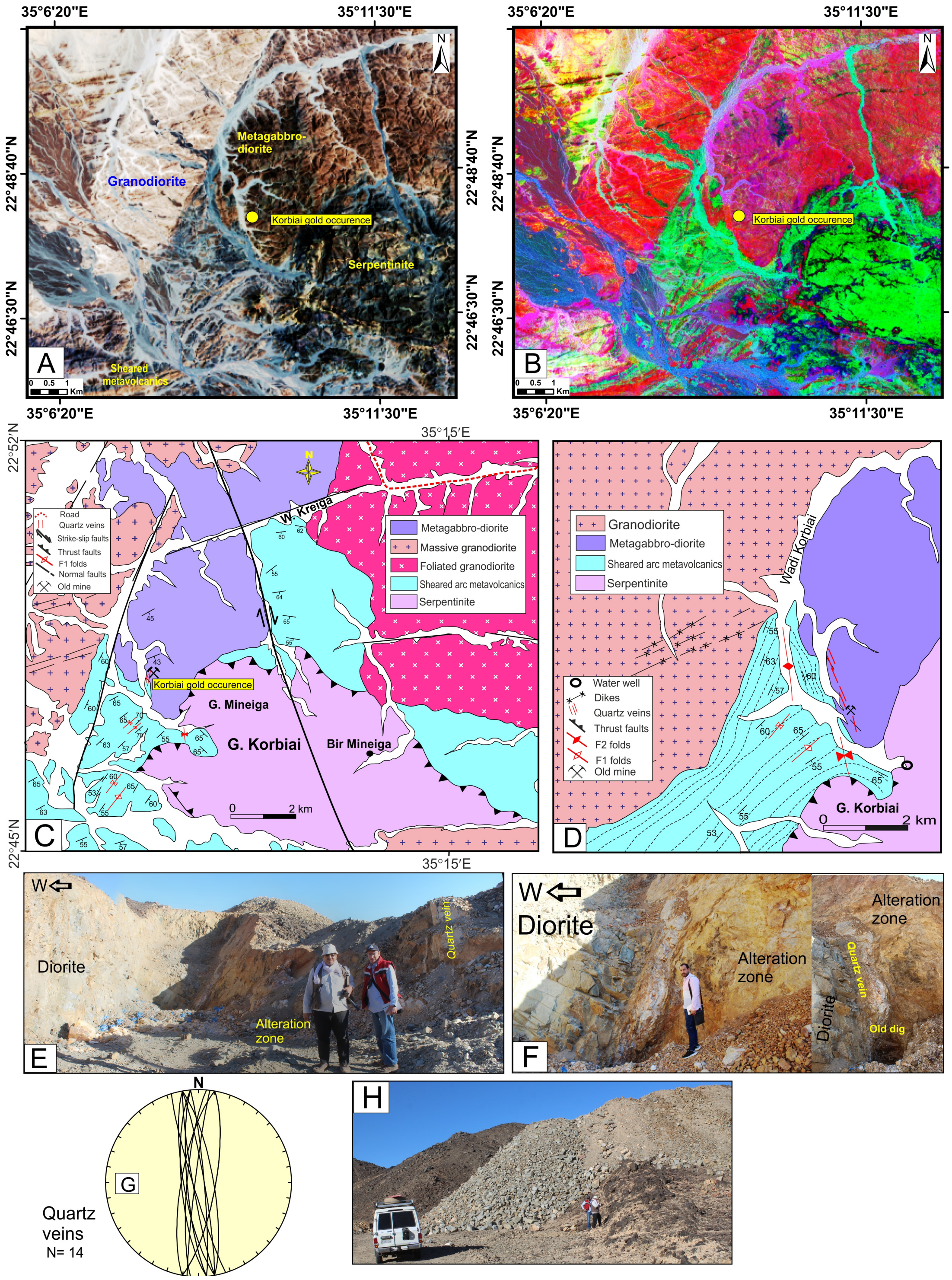

Figure 16. (**A**,**B**) Location of Korbiai gold occurrence on Landsat-8 OLI band composites RGB-753 and Landsat-8 OLI band ratio RGB-7/6 (**C**) Geological map of the area around the Korbiai gold occurrence (modified after EMRA, 2012), (**D**) Detailed geological map of the Korbiai gold occurrence (modified after EMRA, 2012), (**E**) The alteration zone in the Korbiai gold mine along the contact with diorite. The alteration zone is characterized by the presence of recrystallized quartz pods, fracture-filling ankerite, sulfidized granitic offshoots, boudinage of the granodiorite bodies, and intermingling carbonate sericite veinlets, (**F**) Old digging along W-dipping quartz vein marking the contact between diorite and the alteration zone of the Korbiai gold mine, (**G**) The black lines are the great circle plots of the quartz veins in the Korbiai gold occurrence (**H**) Recent excavation and rock smashing at Korbiai gold mine.

Along the shear zones, the serpentinite bodies are transformed into talc-carbonate rocks. The meta-andesite, basaltic andesite, and intermediate to acidic tuffs make up the strongly foliated metavolcanic rocks. In less deformed types of metavolcanic rocks, large boudins and well-developed pencil cleavage are typical. The sheared metavolcanics are intruded by syn-orogonic metagabbro-diorite to monzogranite with variable degrees of shearing. The NNW-trending F2 folds in sheared metavolcanics are asymmetric, and symmetric with high amplitudes and large wavelengths. The S3 foliation in the sheared metavolcanics and metagabbros, strike NE-SW and dip moderately to steeply toward SE and less common to NW. Mineral stretching lineations plunge moderately toward SSE. The NE-trending F3 folds are mainly tight and overturned and preserved in sheared metavolcanics. The WNW-trending F3 folds are of low amplitude, parallel geometry, and occur in kinked metavolcanics. The transpressional imbricate thrusts define the contacts between serpentinites and sheared metavolvanics.

Gold mineralization is restricted to mineralized shear zones, and the bleached sheared host rocks are limited to the SE-steeply dipping shear zones between carbonatized serpentinites and the subordinate ferruginated metavolcanics as well as along the intruded contact between the metagabbros and the sheared metavolcanics. There is significant shearing and alteration in the areas where the granodiorite sends offshoots into the gabbroic rocks, as well as many quartz veins and felsic dykes. Alteration zones and quartz veins are often under the control of N-S shear/fault sets, with the shearing in the region being primarily brittle and seeing minimal ductile deformation. These zones are distinguished by a variety of recrystallized quartz pods, sulfidized granitic offshoots, fracture-filling ankerite, boudinage of the granodiorite bodies, and interspersed carbonate sericite veinlets (Figure 16B,C). Serpentines, sheared metagabbros, and severely sheared metavolcanics make up the majority of these carbonatized shear zones. These shear zones have almost vertical, anastomosing, kinked, crenulated, and foliated fabric that wraps around the stiff serpentinite blocks. Close to the quartz veins, the granodiorites are remarkably sericitized and silicified (quartz–sericite rocks), plagioclase change to sericite and kaolinite and pyrite occurs as the most common alteration mineral dispersed in the hydrothermally altered granitoid and gabbroic rocks.

At the Korbiai occurrence, gold mineralization is restricted to quartz veinlets with up to 5 cm thickness that are encased in quartz diorite intrusion at the interface with sheared metavolcanics (Figure 16C). The sub-vertical NE and ENE striking milky quartz veins reach up to 200 m in length. The main lodge is a stockwork of 40 cm broad veinlets that is surrounded by wall-rock that has undergone hydrothermal alteration, resulting in a mineralization zone that is about 1 m wide. As fills in the microfractures, gold is found in these veinlets and the hydrothermally altered wall-rock (Figure 16B,C). The system of mineralized quartz veinlets is NNW-SSE orientated and steeply dips in the E and W directions. Old sieve terraces (Figure 16D) may be found at several locations within the Korbiai gold deposit, all of which are on low relief sheared metavolcanics. Sand with thicknesses of up to 8 m and unconsolidated conglomerates make up the old, sieved terraces [78].

6.2. Madari Gold Occurrence

The Madari gold occurrence is situated 85 km southwest of the Shalatien city in the region bounded by Lat. 22°30′29″–22°32′33″N and Long. 35°08′48″–35°11′44″E, southwest of G. Gerf and west of G. Madari. It is located in a low relief area and is accessible via the Shalatien-Sohain Asphaltic Road, which is 15 km southeast of G. Korab Kansi (Figure 2).

Lithologicaly, the Madari gold occurrence area is composed of ophiolitic rocks, that are thrust over intermediate to basic metavolcanics and comprise serpentinites, talc carbonate, and gabbroid rocks (Figure 17A). The region contains a particular collection of sheared metavolcanics, mostly with felsic to intermediate composition and locally with a basic composition. The serpentinites of the Madari occurrence occur as an E-W elongated mass thrust over the sheared metavolcanics and gneisses and intruded by syn-orogenic metagabbro-diorite. The contact between the serpentinites and the enveloped sheared metavolcanics is controlled by thrust planes and marked by graphite, chlorite, and talc schists, and carbonate-rich rocks. The sheared metavolcanic rocks are weakly to intensely foliated and converted to tremolite–actinolite and chlorite schists along shear zones.

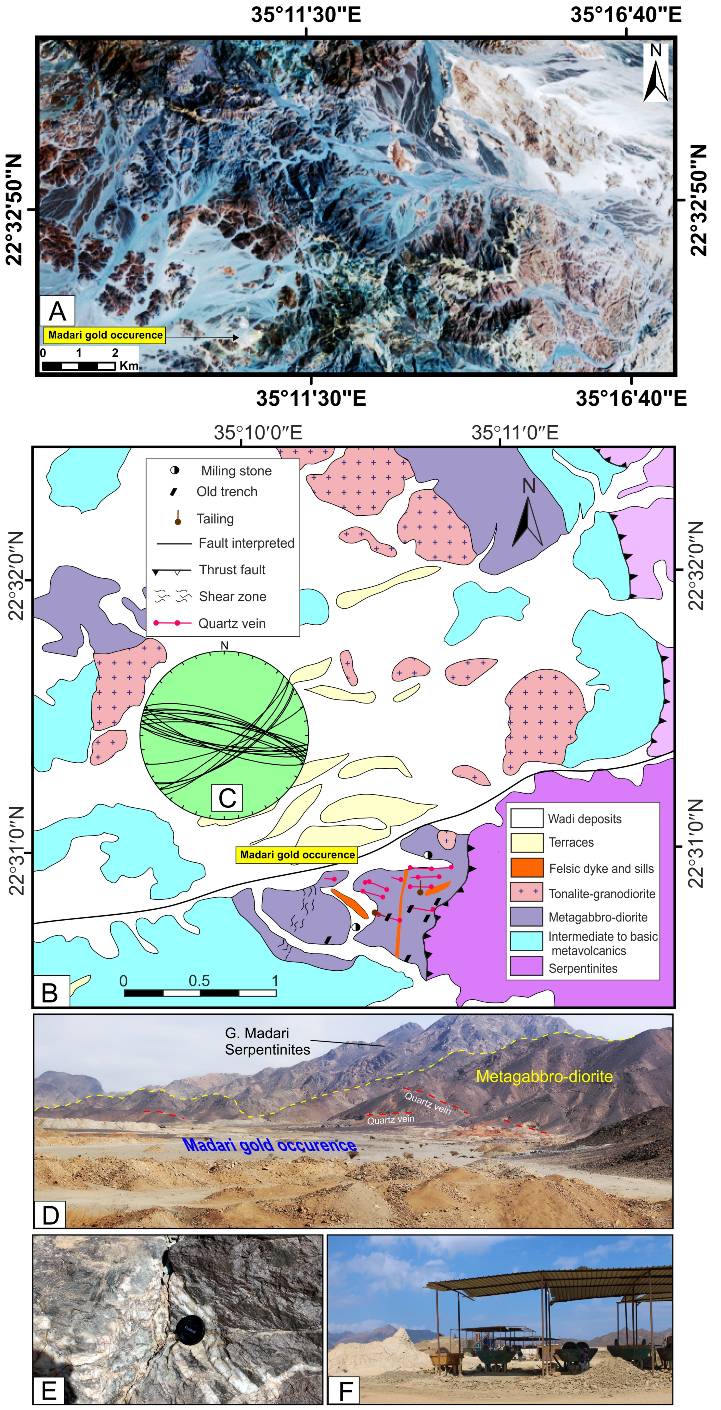

Figure 17. (**A**) Location of the Madari gold occurrence on Landsat-8 OLI band composites RGB-753, (**B**) Geologic map of the Madari area (modified after [88]), (**C**) The black lines are the great circle plots of the quartz veins in Madari gold occurrence, (**D**) The recent gold-mining works in Madari occurrence are limited to brecciated, smokey and high-grade quartz veins that are enclosed in metagabbro, (**E**) Quartz folded to asymmetric isoclinal fold in metagabbro of Madari occurrence, (**F**) Milling stones and gold-mining works in Madari occurrence.

The Madari gold occurrence is structurally located in a kilometer-scale imbricate thrust system to the northern extension of the Hamasina shear zone (Figure 17A). The D2 thrusts that are orientated NNW bind the serpentinites and dip either moderately or steeply to the ENE. Sheets and slices of serpentinites interlock and thrust over metavolcanics. Top-to-NNW thrusting is indicated by asymmetries in anastomosing, kinked textiles, asymmetries in bent quartz lenses, subvertical slickensides, and drag folds.

Gold mineralization is found in Madari in a variety of smoky and white quartz veins, however, not all of them are mineralized. They are also pierced by felsic porphyry dikes, which are occasionally low-grade, sometimes barren, and located nearby the smoky veins (74,75,83,88). These felsic porphyry dikes are distinguished by high silica, biotite, and sericite alterations. There are two trends of the smoky quartz veins reported in the Madari gold occurrence (Figure 17B); these are (i) NE-SW striking and dipping 65° toward SE (10–50 cm thick) and exposed as sheeted veins always hosted within the syn-tectonic gabbro-diorite; (ii) WNW-ESE striking and dipping 70° to NNW mainly related to the post mineralization N-S Hamisana shear zone and are not mineralized. Most of the quartz veins are steeply dipping, sheared, and brecciated and show the banding features. The strongly tectonized gabbro and diorite, which are located near serpentinites, have strongly kaolinitized and oxidized zones.

High-grade quartz veins are found in low-relief, heavily weathered, altered gabbro-diorite intrusions in the Madari area (Figure 17C). Old gold-mining operations (Figure 17D) can be found in wedged quartz pods and lenses, high-angle reverse ductile-brittle shear zones, asymmetric isoclinal folds, and folds intersecting cleavages.

Lode gold deposits are found in quartz veins and wall rocks as discrete and dispersed gold with trace amounts of pyrite, arsenopyrite, and chalcopyrite. Some areas where the wall rocks near to the quartz vein have undergone significant silicification, chloritization, and pyritization as a result of the percolation of external hydrothermal fluids may have undergone a metasomatic alteration [84]. Numerous quartz veins with banding patterns, are sheared and brecciated, and often dip sharply.

The recent gold-mining works in Madari occurrence are limited to brecciated smokey quartz veins that are encased in metagabbro (Figure 17C,E) and sheared metavolcanic rocks. Many quartz veins containing gold were mined in antiquity. Gold-bearing quartz vein system with thicknesses ranging from 0.1 m to 0.3 m extends up to 600 m in WNW-ESE and NE-SW. The region also has abandoned gold placer mining operations, numerous dumps, little tailing, historic mills, and crude stone houses [78]. According to Oweiss et al. [89], Madari gold mineralization is restricted to a sequence of black to grey quartz veins that stretches up to 1800 m along strike in the E-W and NE-SW axes.

7. GIS-Based Gold Potentiality Mapping

One of the most efficient methods for identifying the high-potential gold mineralized zones has been the integration of several data types such as lithological, structural, and remote sensing findings. In order to give comprehensive information regarding the gold mineralization zones in the Gerf area, the current study combined a number of different datasets. This can help to guide to locate the high probability of undiscovered gold mineralization areas. GIS multi-criteria model has been successfully used in the current study to integrate the geological features, field data, structural analysis, and results of processed remotely sensed techniques to locate these high potential zones for gold mineralization.

It is known that the main criterion of gold exploration is the host lithology, structures, and hydrothermal alteration zones. In order to create a geographic model, multisource datasets were acquired, examined, and combined. The high potential zone of gold mineralization was located using eight theme layers, each of which contributed in a different way. These thematic maps are geology, alteration zone, major faults, linear structures, and the gold-bearing quartz veins (Table 6). They are the outputs of the processed remotely sensed data of the two sensors optical and radar, as well as the structural analysis (Table 6). To meet the requirements of the weighted overlay model, all of these layers were standardized.

They share the same cell (pixel) size and geographic projection in a categorized raster format [90]. As a result, using ArcGIS' "feature to raster" function, all vector layers related to geology, faults, and lineaments were first converted to raster types. Then, each raster layer was subjected to the "Euclidean distance" spatial analysis tool to provide a classed map with a buffer distance around the mapped feature, such as faults, mineralized quartz veins, and ancient gold occurrences. All acquired raster maps were recategorized and ranked from 1 to 5 into five classes (where 5 is the most favorable). The weighted overlay analysis might begin with the eight rated layers (WOA). Depending on the number of thematic layers, WOA is one of the Multi Criteria Decision Analysis (MCDA) techniques that are most successful. Depending on its proportional significance compared to the other implemented levels, each thematic layer is given a weight. All theme layers' given weights must add up to a total of 100. The layers were then analyzed using the ArcGIS Spatial Analyst tool and the "Model Builder" analytical tool to organize the allocated gold occurrences on a knowledge-based hierarchy. The research region was divided into four relative zones, labeled as low, moderated, high, and very high prospective zones on a map that was created to show the potential for gold mineralization (Figure 18). The produced map indicates that very high potential zones coincide with the alteration zone maps of Figure 19A,C. These high potential zones are confined to contacts of the ophiolitic rocks (serpentinite, ophiolitic metavolcanics, and ophiolitic metagabbros), arc metavolcanic, and metagabbroic rocks. It is apparent that the three gold occurrences (G. Gerf, G. Madari, and G. Korbiai) reported by El Naggar et al. [77] and El Shimi et al. [78] are situated in areas with high and extremely high potential. The thrust and strike slip faults' primary trends appear to correlate with the extremely high potential zone. In order to strongly suggest attractive mineralized gold locations, highly weighted values are believed to be the collective representation of host lithology, structural complexity, and alteration zones. The new gold potential map indicates that still there are promising areas for gold exploration in the Gerf area, especially since the high and very high potential zones cover about 53% of the study area. One of these new promising sites is G. Korab Kansi needs more attention in the future gold exploration in the Gerf area.

Table 6. Weights assigned for different gold mineralization parameters in the study area.

Thematic Layer	Class Ranges	Layer Weight	Influence (%)	Class Rank	Data Source and Technique
Favorable host lithology	sp/omv/omg/mg	0.30	30	5	L 8 and S2B processed using FCC, BR, PCA, MNF, and MLC
	amv/mz			4	
	ms/sgr/mgr			3	
	lgb			2	
	gn			1	
Alteration zones map	Argillic (K., Mont., Illite)	0.20	20	5	L 8 and ASTER processed using BR, mineral indices and CEM
	Propylitic (Epidote, Chlorite)			4	
	OH-bearings rocks			3	
	Ophio-carbonates (calcite, Talc)			2	
Proximity to mineralized quartz veins (km)	<1	0.10	10	4	Previous work processed by ArcGIS
	1–3			3	
	>3			2	
Proximity to thrust faults (km)	<1	0.10	10	3	Processed L 8 and S2B images and fieldwork
	1–3			2	
	>3			1	
Proximity to old gold mines (km)	<10	0.09	9	3	Previous work processed by ArcGIS
	10–20			2	
	>20			1	
Proximity to favorable contacts (km)	<2	0.08	8	3	L 8 and S2B processed using FCC, BR, PCA, MNF and MLC
	2–10			2	
	>10			1	

Table 6. *Cont.*

Thematic Layer	Class Ranges	Layer Weight	Influence (%)	Class Rank	Data Source and Technique
Lineaments density (km/km^2)	1.7–1.9	0.07	7	5	Produced using the spatial analyst function included in ArcGIS
	1.3–1.6			4	
	0.79–1.2			3	
	0.4–0.78			2	
	0–0.39			1	
Major faults density (km/km^2)	1.14–1.41	0.06	6	5	Produced using the spatial analyst function included in ArcGIS
	0.85–1.13			4	
	0.57–0.84			3	
	0.29–0.56			2	
	0–0.28			1	

K = kaolinite, Mont. = montmorillonite, for lithology abbreviations (see Figure 5).

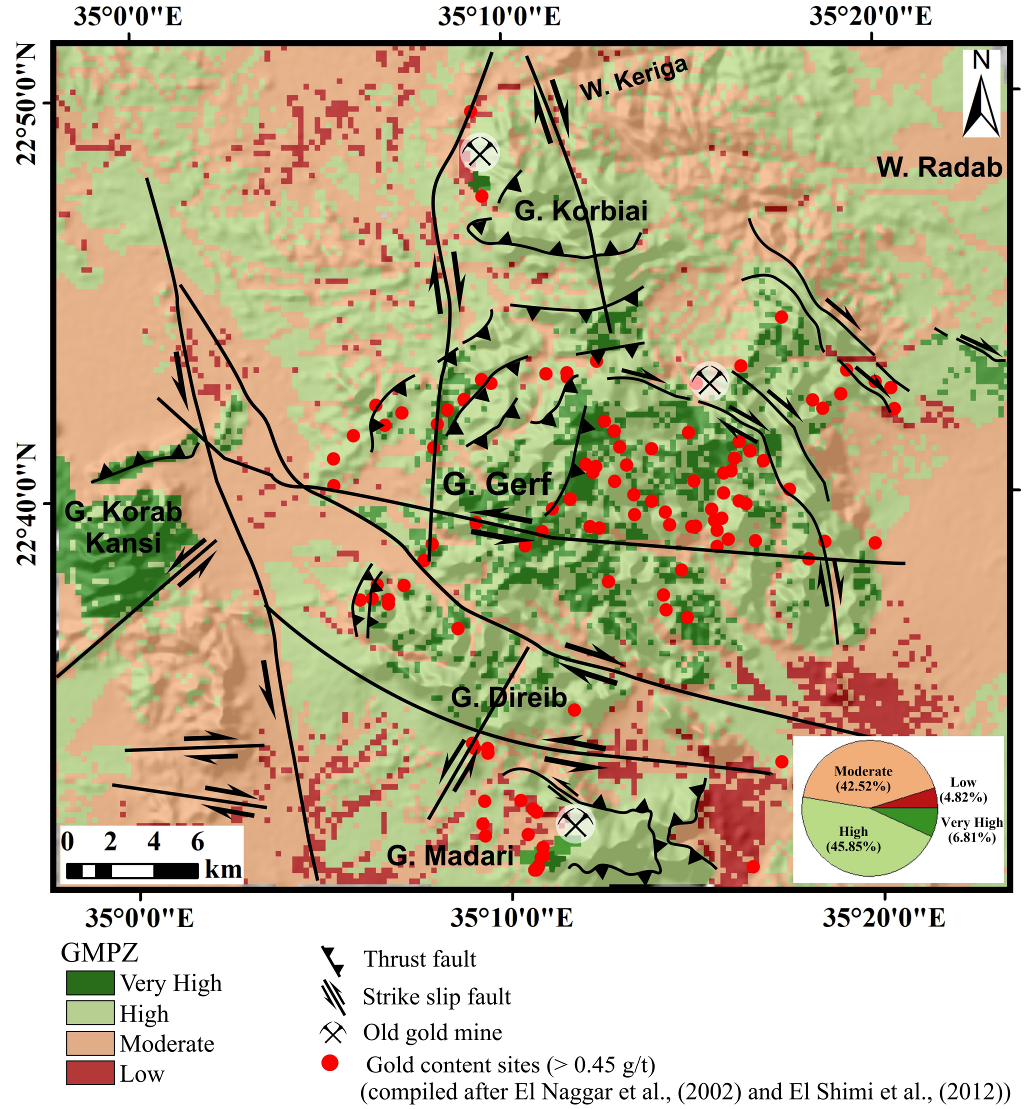

Figure 18. The Gold mineralization potential zones map, (inset circle shows the percentage of each potential zones. The gold content sites are complied after [77,78].

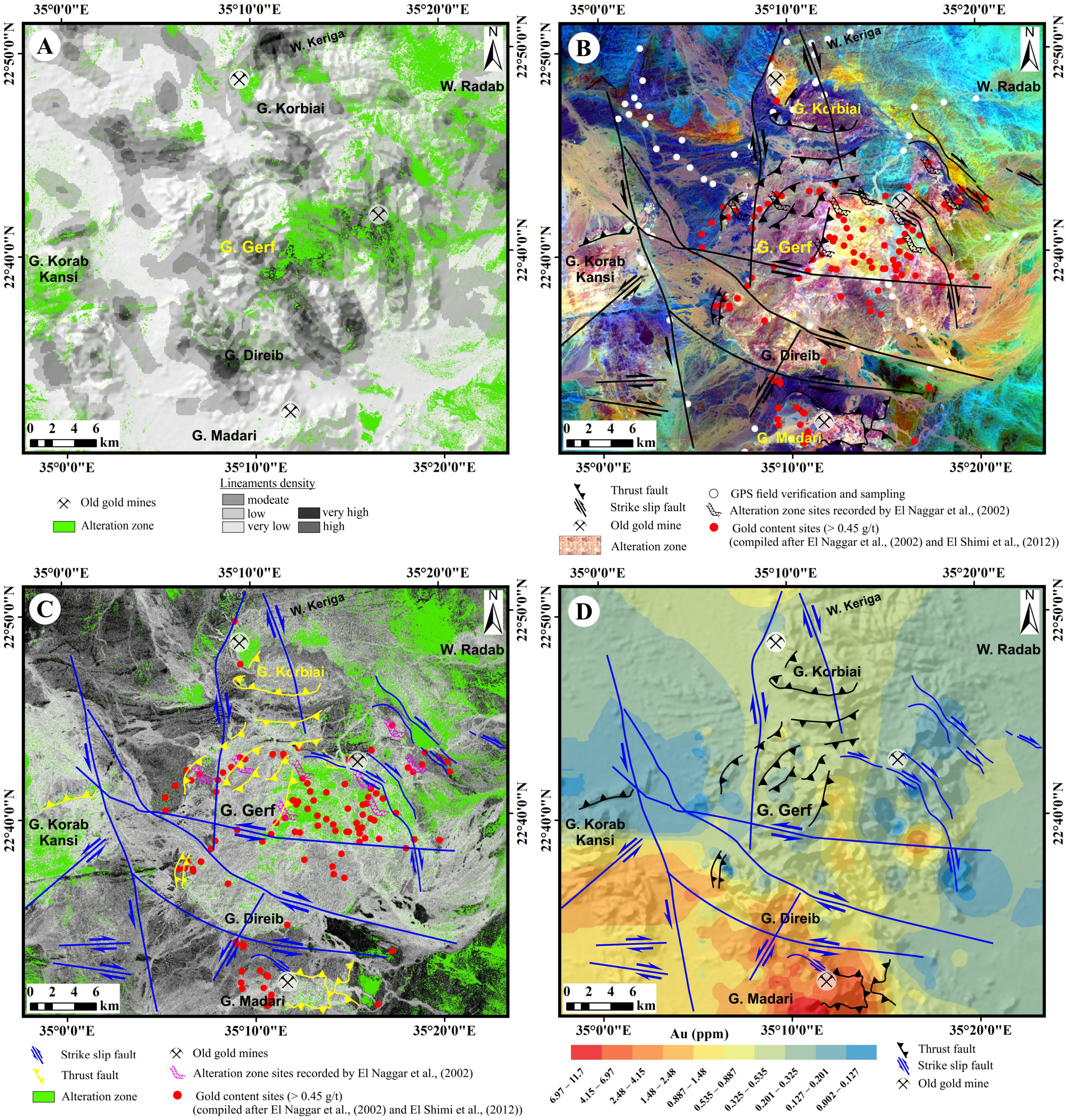

Figure 19. (**A**) The alteration zones in relation to the lineaments density maps, (**B**) Fused image of KLI, ALI, and CLI to locate the alteration zone in whitish yellow color, (**C**) The spatial distribution of the alteration zone in relation to the major structural elements, (**D**) The gold content distribution in the study area based on the data after [77,78].

8. Discussion

8.1. Lithological and Alteration Zones Mapping

In this work we have used several remote sensing improvement techniques, including FCC, BR, PCA, MNF, and MLC, to provide an updated geologic map. These techniques are applied to three different optical datasets of Landsat-8, S2B, and ASTER. The FCC 753 in RGB of Landsat-8 and FCC 11–12-8 in RGB of S2B highlighted the ultramafic and mafic rocks from the other units such as arc metavolcanics, syn-tectonic intrusions and late-tectonic intrusions (Figure 5A,B). The band ratios of Chica–Olma (6/7, 6/5, 4/2 in RGB), Kaufmann (7/5, 5/4, 6/7 in RGB) and S2B (12/11, 8/6, 12/6 in RGB) differentiated the rock units in the study area (Figure 5C–E, respectively). The contact between the ophiolitic assemblage (serpentine, ophiolitic metavolcanics, and ophiolitic metagabbro) and the surrounding rock units could be successfully discovered due to the high interference color of the ophiolitic rocks in these ratios. Chica–Olma band ratio enhances the alteration zone in faint yellow color. In addition, the foliated rock units such as arc metapyroclastic, metavolcanics, and layered gabbros are manifested by the alternative colors of the foliation trajectories due to the variation in the mineral composition. The folding form in these rocks could be visually detected and traced. The granitic and gneissic masses are distinguished by a ramp of faint colors of orange and cyan. Depending on the eigenvectors and loadings values, the present study performed PCA-432 in RGB and MNF-421 in RGB for Landsat-8 data (Figures 5F and 6A) and MNF-432 for the S2B (Figure 6B). Three colorful images provided extensively successful discrimination of the different rock units in the study area. Figures 5F and 6B highlighted reasonably the foliated rock units such as arc metapyroclatics and metavolcanics, whereas Figure 6B discriminated the serpentinites as a high-relief green color from the yellow color of the ophiolitic metavolcanics.

To discriminate between the ultramafic-mafic rocks and the surrounding SiO_2-rich rocks, the present study adopted the mafic index (MI = B13-0.9147) × (B10-1.4366) and BR of SiO_2 = 13/12 to the ASTER data (Figure 6C,D). The mafic index (Figure 6C) provided the ultramafic-mafic rocks as bright pixels and outlined the ophiolitic rocks accurately, whereas the SiO_2-bearing rocks such as granitic and gneissic masses were separated from the mafic rocks by using the band ration of the thermal bands of ASTER of 13/12. Ge et al. [66] introduced an effective band ratio using bands 3 and 12 of S2B and bands 8 and 9 of ASTER as (S1B3 + A9)/(S1B12 + A8) to delineate the serpentinite (Figure 6E,F). The present study adopted this ratio because serpentinite is the most favorable host rock of the gold mineralization. Above mentioned data results are used as a base to build a training areas file to perform MLC classification and produced a classified geologic map with 89% accuracy (Figure 7). The machine learning classification (e.g., MLC) has successfully enabled mapping of the Precambrian rocks in the Eastern Desert of Egypt with high accuracy e.g., [91,92].

Moreover, to demarcate the alteration zone in the study area, specific BR and mineral indices were applied. The hydroxyl-bearing minerals are detected using the BR 6/7 of Lndsat-8 and OHI, whereas the kaolinite and alunite which characterize the argillic alteration zone were detected using KLI and ALI indices, respectively. Propylitic alteration and its characteristics calcite mineral were detected by applying the CLI index. The grey scale produced images marked effectively the hydrothermal alteration zones and associated minerals. The most common CEM-supervised classification technique performed on the ASTER data enabled the allocation of the spatial distribution of the seven most important alteration minerals such as kaolinite, montmorillonite, illite, chlorite, epidote, calcite, and talc which identify the three alteration zones of argillic, phyllic and propylitic. CEM enables the identification of the spatial distribution of these minerals and enhances their concentration zones (Figure 10A–D).

The findings of the alteration zones based on the ASTER, Landsat-8, and S2B datasets demonstrate the spatial association of highly sheared rocks with gold occurrences that overlap on the old working gold occurrences associated with the highly deformed and fractured zones surrounding the tectonized ophiolitic belt, thrust contacts, and within syntectonic gabbro-diorite intrusions such as the Korbiai and Madari gold mines. Therefore, in addition to thorough fieldwork examination, the Landsat-8 OLI, S2B, and ASTER datasets were useful for determining the alteration zones related to orogenic gold mineralization in the study region together with the detailed structural and lithological mapping. A false-color composite (FCC) ratio image was created by combining the three grayscale mineralogical indices images of OHI, KLI, and CLI in the RGB channels (Figure 19B), in which the alteration zone appears as whitish yellow to whitish purple colors. The ophiolitic and island arc rocks, which are strongly tectonized in the studied region, as well as the ductile deformation zone, are linked to the hydrothermal alteration zones. Highly sheared rocks are spatially associated with gold occurrences, according to the results of alteration mapping generated from the ASTER, Landsat 8, and S2B datasets.

8.2. Integration of Mineralization to Lineament and Structural Elements

The Radar data of PALSAR and Sentinel-1B were used as a source to extract the lineaments automatically. The extracted lineaments exhibit the dominant trends of NW–SE, N–S, E–W, and NE-SW orientation. These trends coincidence mostly with the major thrust, strike-slip faults and constitute a favorable site for the gold mineralization in the study area. To show highly dissected regions and improve the results of visualization, two lineament density maps were made.

The highest lineament density may indicate a greater degree of rock fracture that is associated with mineralization. Lineaments and cracks are regarded as important conduits for hydrothermal solution fluid movement. The likelihood of gold mineralization potential is increased by the high density of lineaments/fractures linked with hydrothermal modifications zones. As a result, the lineament density map of the research region has the modification zones that have been effectively delimited using the CEM approach draped over it (Figure 19A). The geographical distribution of the alteration zones and the regions of the lineaments with extremely high densities are very well matched, indicating the significance of these lineaments in the mineralization process. The most likely mineralization zones in the research region could be found by careful examination of this map (Figure 19A).

The Red Sea mountains share the same linear features as mineralization zones [93–95]. Abd El-Wahed et al. [13] suggested that the gold mineralization-related shear zones in the Wadi Hodein area north of the present study are controlled basically by the major thrust faults and fractures which act as the favored channels for fluid migration. Therefore, the high-density lineaments/fractures are often localized close to mineralization zones [96]. The present study generated two maps to explore the close spatial relation between the structural elements, alteration zones, and gold occurrences in the study area. Figure 19B is the fused image of KLI, ALI, and CLI mineral indices which demarcated the alteration zone with whitish-yellow color. Figure 19C shows the spatial distribution of the alteration zone minerals identified by the CEM technique in relation to the structural framework of the study area. Figure 19B–D confirmed with a high level of confidence the great spatial agreement between the alteration zones, in the meantime the gold mineralization, and the thrust and strike slip faults in the study area. El Naggar et al. [77] recorded many localities of alteration zone in the G. Gerf area, and they mentioned that these localities have two types of alteration zones: one associated with serpentinites and the other with metavolcanics. The validation of the resultant maps in Figure 19A,B is carried out by a good matching of the locations of the alteration zones of El Naggar et al. [77] and the produced alteration zone from the present study. In addition, 117 samples containing gold complied from El Naggar et al. [77] and El Shimi et al. [78] are located over the two resultant maps (Figure 19B,C). The distribution of these samples and their associated gold contents are confined to the alteration zone and along the thrust faults and contacts. Consequently, the gold mineralization in the study area is structurally controlled and related to the thrust shear zones. These shear zones can therefore be used as an indicator of the potential gold mineralization in undiscovered areas. The gold content of these samples is interpolated in Figure 19D to explore the spatial distribution of the gold concentration in the study area and its relation to the structural elements. It is indicated that the high gold content is recorded around G. Madari in the south of G. Gerf and gradually decreases to the north. Also, the high gold content seems to be confined by the major thrust faults.

8.3. Data Integration and Validation

It has become known that the exploration of potential gold mineralized zones needs an integration of multiple datasets and studies. Considerable lithologic mapping, detailed structural analysis, processing of the remotely sensed data, and intensive fieldwork were performed in the present study to identify areas of potential gold mineralization. The integration of the used datasets results manifests their efficient role in robust recommendations for the new expected zones of gold mineralization. Therefore, all the produced maps (MLC classified map, alteration zone maps, and the gold potential mineralization zones map) were subjected to the validation process. Comprehensive geological fieldworks were carried out in December 2020 and December 2022 to investigate the lithological units, make serious structural measurements and analysis and visit the alteration zones areas and the old gold occurrences. The rock samples and the petrographical investigation were used to validate the final geologic map produced from the remote sensing data (Figures 2 and 7). The field investigation of the alteration zones with the ophiolitic assemblage and metavolcanics as well as the recorded alteration zones in the prior literature were used to validate the alteration zones extracted from the mineral indices and CEM technique (Figure 19B,C). It found that the alteration zones recorded by El Naggar et al. [77] in the study area are located and matched with the alteration zones maps produced in the present study. Finally, the gold mentalization potential map (Figure 18) was validated with 117 GPS gold occurrence points documented by El Naggar et al. [77] and El Shimi et al. [78] (Figure 18). It can be observed that the locations of 72 points fall within the very high potential zone and 33 points fall within the high potential zone with a sum of 105 points out of the 117 points located in areas having high and very high potentiality for gold mineralization (Figure 20). The validation process of the gold mineralization potential zone map is summarized in Table 7 and presented in Figure 18. The obtained results of the validation confirm the usefulness and effectiveness of applying remote sensing and structural studies in the gold exploration process. Therefore, the present study shows that the adopted methodology can be followed for mapping the gold-favorable mineralized zones in similar geologic settings.

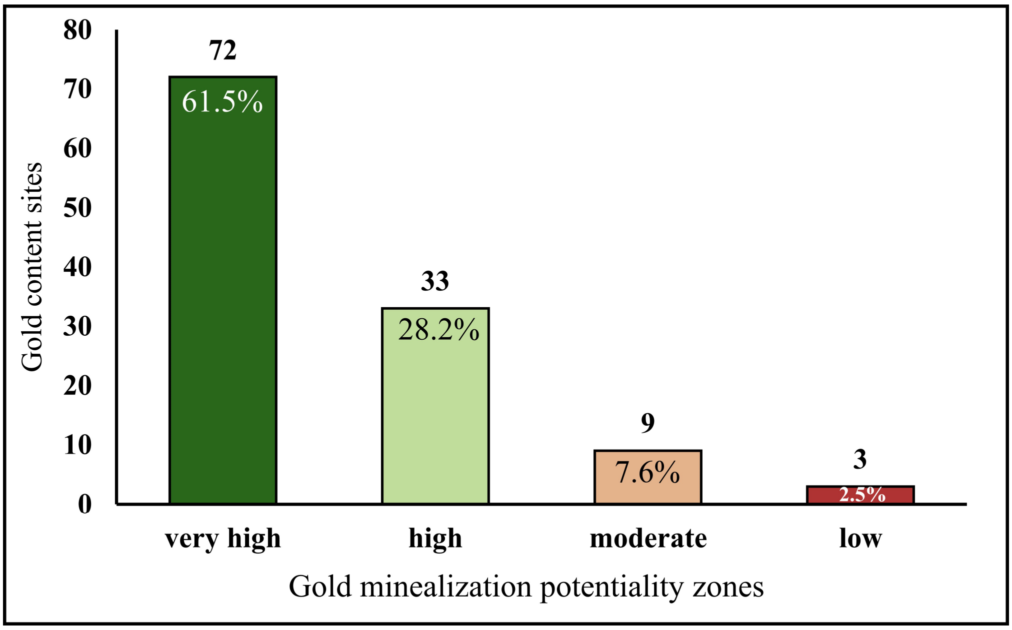

Figure 20. The results of the validation process of the gold mineralization potential zones map.

Table 7. The validation gird points to the gold mineralization potential zones map.

Zone	Very High	High	Moderate	Low	Total
Gold content sites	72	33	9	3	117
Percent (%)	61.5	28.2	7.6	2.5	100

8.4. Tectonic Evolution of Gerf Area

The thrust-dominated shortening or shortening accommodated by thrust and strike-slip shear zones is considered the dominate force that affected the Gerf area. Theoretically, the Gerf area is surrounded by two major sinistral shear zones; (i) Extension of NW-striking Kharit-Hodein shear zone [97] and (ii) Concealed shear zone west of Gerf nappe. Movement along these shear zones shaped the structure of the Gerf area that evolved throughout three deformation phases (D2, D3 and D4). The E–W oblique convergence and the transpressional D2 phase are evolved during the collision between East and West Gondwana which accommodated by the N-S trending Hamisana shear zone where its northern parts are exposed in the Gerf area along W. Moderal and W. Kwat Hawa. Thrust-dominated transpressional D2 structures include N-S trending S2 and L2 rock fabrics as well as the tight and overturned F2 folds with the N/NNW-steeply plunging fold axes. Thrusts formed during D2 are exposed as W/WSW-propagated imbricate and piggy-back thrusts that are responsible for the refolding of the early F1 folds. D2 is characterized by syn-tectonic magmatic intrusions of gabbro-dioritic and granodioritic rocks which cut through the ophiolitic and arc-assemblages rocks.

Subvertical NNW-Striking foliation (S3), NNW-SSE thrust-dominant strike slip shear zones, and NNW- and ENE-trending folds (F3) were generated by post-accretionary E-W shortening (D3). A crenulation lineation with a sub-horizontal descent to the NNW or SSE is the L3 lineation. Also, D3 developed the NNW-plunging stretching and mineral lineations (L3), NNW-verging large thrusts, E-W striking S3 regional foliation, S3m mylonitic foliation, F3 massive kilometer scale anticlines and synclines, and minor open, asymmetrical to isoclinal folds. A sequence of large-scale folds (F3) connected to NNW-vergent foliation (S3) serves as a representation of the main D3 fabrics, showing that the F3 folds developed in reaction to the deflection and rotation of S2 and F2 as deformation progressed. Series of NW- and NE-striking strike-slip faults as well as the late-magmatic intrusions of layered gabbro and monzogranites are the main characteristics of D3.

9. Conclusions

The understanding of the litho-tectonic settings of the shear-related gold mineralization in the southern Eastern Desert of Egypt has taken the attention of many workers in the last few years. The use of remote sensing capabilities in lithological mapping, detecting the structural features, and identifying the alteration zones has been helpful in investigating the spatial distribution of the gold occurrences in the highly deformed ophiolitic blocks in this area. Accordingly, the present study adopted a multispectral remote sensing data processing workflow coupled with structural and field investigations to produce a credible gold mineralization potential zones map to the Gabal Gerf area. Remote sensing enhancement techniques including, band combinations (FCC), band ratioing (BR), Principal Component Analysis (PCA), Minimum Noise Fraction (MNF), and Maximum Likelihood Classifier (MLC) were applied on Landsat-8 and S2B datasets to produce an updated geologic map to the area. Special attention was paid to the ophiolitic assemblage that is considered the target lithology of the gold mineralization in this region. The mafic index (MI) = (B13-0.9147)x(B10-1.4366) of the ASTER thermal bands and a distinctive band ratio of S2B and ASTER of (S2B3+A9)/(S2B12+A8) were effectively successful in differentiating the ophiolitic assemblages and their thrusted contacts. Different mineral indices and CEM mineral mapping techniques accurately identified argillic, phyllic and propylitic alteration zones that are related to gold mineralization.

On the other hand, the PCA and filtering techniques applied to S1B and ALOS PALSAR datasets enabled a detailed mapping of the major lineaments and deciphering the regional structural features. The structural field investigation revealed that the area has been subjected to three main phases of deformation; (i) NE-SW convergence and sinistral transpression (D2); (ii) ~E-W far field compressional regime (D3), and (iii) extensional tectonics and terrane exhumation (D4). The superimposed ductile and brittle deformation fabrics observed in the Gerf ophiolitic and island arc rocks may imply a voluminous shear-derived fluid circulation which helped the formation of gold during the transpression increments.

Analysis of the remote sensing results assessed by the structural interpretation revealed that the alteration zones in the study area are confined to the thrusted contacts between serpentinites, metavolcanics, and gabbro-diorite complex. These contacts are considered favorable sites for gold mineralization. The successful correlation among host lithology, alteration zones, and high-density ductile-brittle structural zones are points to exploration targets for gold mineralization in the study area. These results are supported by the observation that the gold mineralization at the Korbiai gold mine to the north are confined to the NNW trending shear zones and that the gold-bearing quartz veins at Madari gold mine to the south of the area are controlled by NE-SW dextral brittle ductile shear zones of the D3 structures.. Finally, weighted overlay analysis performed on all thematic output maps enabled the production ofa gold prospectivity map with very high to high priority gold mineralization zones. This map could aid the future exploration of gold mineralization in the study area which that may be supported by geochemical analysis.

Supplementary Materials: The following supporting information can be downloaded at: https://www.mdpi.com/article/10.3390/rs15081974/s1, Figure S1: Photomicrographs for some selected rocks from Gerf area; (a) Biotite gneiss consists of biotite, quartz and plagioclase, (b) Thin-section views of serpentine minerals and talc carbonates, (c) Serpentinized peridotite composed of serpentine minerals surrounding the orthopyroxene mineral, (d) Ophiolitic metagabbro composed of hornblende and plagioclase, (e) Altered plagioclase phenocryst in the metabasalt, (f) Euhedral plagioclase in the metaandesite, (g) Hornblende schist consists of hornblende, plagioclase and quartz formed, (h) olivine gabbro mainly composed of plagioclase, olivine and pyroxene forming typical ophitic texture, (i) Mozongranite composed mostly of quartz, alkali-feldspar and plagioclase, with subequal amounts of plagioclase and alkali-feldspar, (j) Syenogranite composed mostly of quartz and alkali-feldspar and plagioclase, with plagioclase usually less than alkali-feldspar, (k) Carbonate-chlorite-epidote schist from the alteration zones to the north of G. Gerf, (l) Mylonitic chlorite schist from the alteration zones to the north of G. Korbiai, Table S1: Summarized features of the PALSAR and Sentinel-1B datasets [30].

Author Contributions: M.A.E.-W. and S.K. designed the study, collected the data and prepared the figures; M.A. processed the satellite images and performed the experiments; M.A.E.-W., S.K. and B.Z. conducted the analysis and drafted the manuscript; A.A., M.A.A., M.H. and E.M.L. revised the manuscript. All authors have read and agreed to the published version of the manuscript.

Funding: This work was supported by Tanta University, Egypt under a project named "Integrated Geological and Geophysical Mineral Exploration Studies on the northern part of the Halayeb-Shalateen Triangle, South Eastern Desert, Egypt". The project code is TU-091901.

Acknowledgments: The authors would like to thank Tanta University for providing the project funding (Tanta University: TU-091901) and the anonymous editor and reviewers whose constructive comments and suggestions have helped significantly improve the quality of this article.

Conflicts of Interest: The authors declare no conflict of interest.

References

1. Stern, R.J. Arc assembly and continental collision in the Neoproterozoic East African Orogen: Implications for the consolidation of Gondwanaland. *Annu. Rev. Earth Planet Sci.* **1994**, *22*, 319–351. [CrossRef]
2. Fritz, H.; Dallmeyer, D.R.; Wallberecher, E.; Loizenbauer, J.; Hoinkes, G.; Neumayr, P.; Khudeir, A.A. Neoproterozoic tectonothermal evolution of the central Eastern Desert, Egypt: A slow velocity tectonic process of core complex exhumation. *J. Afr. Earth Sci.* **2002**, *34*, 137–155. [CrossRef]
3. Fritz, H.; Wallbrecher, E.; Khudier, A.A.; Abu El Ela, F.; Dallmeyer, R.D. Formation of Neoproterozoic metamorphic core complexes during oblique convergence, Eastern Desert, Egypt. *J. Afr. Earth Sci.* **1996**, *23*, 311–329. [CrossRef]
4. Abdeen, M.M.; Greiling, R.O. A quantitative structural study of Late Pan-African compressional deformation in the central Eastern Desert (Egypt) during Gondwana assembly. *Gondwana Res.* **2005**, *8*, 457–471. [CrossRef]
5. Abd El-Wahed, M.A. Thrusting and transpressional shearing in the Pan-African nappe southwest El-Sibai core complex, Central Eastern Desert, Egypt. *J. Afr. Earth Sci.* **2008**, *50*, 16–36. [CrossRef]

6. Fritz, H.; Abdelsalam, M.; Ali, K.A.; Bingen, B.; Collins, A.S.; Fowler, A.R.; Ghebreab, W.; Hauzenberger, C.A.; Johnson, P.R.; Kusky, T.M.; et al. Orogen styles in the East African Orogen: A review of the Neoproterozoic to Cambrian tectonic evolution. *J. Afr. Earth Sci.* **2013**, *86*, 65–106. [CrossRef]
7. Zoheir, B.A.; Emam, A.; El-Amawy, M.; Abu-Alam, T. Auriferous shear zones in the central Allaqi-Heiani belt: Orogenic gold in post-accretionary structures, SE Egypt. *J. Afr. Earth Sci.* **2018**, *146*, 118–131. [CrossRef]
8. Zoheir, B.A.; Feigenson, M.; Zi, J.-W.; Turrin, B.; Deshesh, F.; El-Metwally, A. Ediacaran (~600 Ma) orogenic gold in Egypt: Age of the Atalla gold mineralization and its geological significance. *Int. Geol. Rev.* **2018**, *61*, 779–794. [CrossRef]
9. Zoheir, B.A.; Emam, A.; Abd El-Wahed, M.; Soliman, N. Gold endowment in the evolution of the Allaqi-Heiani suture, Egypt: A synthesis of geological, structural, and space-borne imagery data. *Ore Geol. Rev.* **2019**, *110*, 102938. [CrossRef]
10. Zoheir, B.; Abd El-Wahed, M.A.; Pour, A.B.; Abdelnasser, A. Orogenic Gold in Transpression and Transtension Zones: Field and Remote Sensing Studies of the Barramiya–Mueilha Sector, Egypt. *Remote Sens.* **2019**, *11*, 2122. [CrossRef]
11. Hamimi, Z.; Abd El-Wahed, M.A.; Gahlan, H.A.; Kamh, S.Z. Tectonics of the Eastern Desert of Egypt: Key to understanding the Neoproterozoic evolution of the Arabian-Nubian Shield (East African Orogen). In *Geology of the Arab World—An Overview*; Bendaoud, A., Hamimi, Z., Hamoudi, M., Djemai, S., Zoheir, B., Eds.; Springer Geology; Springer: Berlin, Germany, 2019; pp. 1–81.
12. Abd El-Wahed, M.A.; Lebda, E.; Ali, A.; Kamh, S.; Attia, M. The structural geometry and metamorphic evolution of the Umm Gheig shear belt, Central Eastern Desert, Egypt: Implications for exhumation of Sibai Core Complex during oblique transpression. *Arab. J. Geosci.* **2019**, *12*, 764. [CrossRef]
13. Abd El-Wahed, M.A.; Zoheir, B.; Pour, A.B.; Kamh, S. Shear-Related Gold Ores in the Wadi Hodein Shear Belt, South Eastern Desert of Egypt: Analysis of Remote Sensing, Field and Structural Data. *Minerals* **2021**, *11*, 474. [CrossRef]
14. Abd El-Wahed, M.A.; Attia, M. Genesis of the gneissic core complexes in the Arabian-Nubian Shield and its tectonic implications: A regional overview. *J. Asian Earth Sci.* **2022**, *236*, 105337. [CrossRef]
15. Kröner, A.; Stern, R.J. Pan-African orogeny. In *Encyclopedia of Geology*, 1st ed.; Selley, R.C., Cocks, L.R.M., Plimer, I.R., Eds.; Elsevier: Amsterdam, The Netherlands, 2004; pp. 1–12.
16. Stern, R.J.; Hedge, C.E. Geochronologic and isotopic constraints on Late Precambrian crustal evolution in the Eastern Desert of Egypt. *Am. J. Sci.* **1985**, *285*, 97–127. [CrossRef]
17. El Gaby, S.; List, F.K.; Tehrani, R. Geology, evolution and metallogenesis of the Pan-African Belt in Egypt. In *The Pan African Belt of Northeast Africa and Adjacent Areas*; El Gaby, S., Greiling, R.O., Eds.; Vieweg & Sohn: Braunschweig, Germany; Wiesbaden, Germany, 1988; pp. 17–68.
18. Abd El-Wahed, M.A.; Ashmawy, M.H.; Tawfik, H.A. Structural setting of Cretaceous pull-apart basins and Miocene extensional folds in Quseir-Umm Gheig region, northwestern Red Sea, Egypt. *Lithosphere* **2010**, *2*, 13–32. [CrossRef]
19. Abd El-Wahed, M.A.; Harraz, H.Z.; El-Behairy, M.H. Transpressional imbricate thrust zones controlling gold mineralization in the Central Eastern Desert of Egypt. *Ore Geol. Rev.* **2016**, *78*, 424–446. [CrossRef]
20. Abu-Alam, T.S.; Stüwe, K. Exhumation during oblique transpression: The Feiran-Solaf region, Egypt. *J. Metamorph. Geol.* **2009**, *27*, 439–459. [CrossRef]
21. Abd El-Wahed, M.A.; Kamh, S.Z. Pan African dextral transpressive duplex and flower structure in the Central Eastern Desert of Egypt. *Gondwana Res.* **2010**, *18*, 315–336. [CrossRef]
22. Abu-Alam, T.S.; Abdel El Monsef, M.; Grosch, E. Shear-zone hosted gold mineralization of the Arabian-Nubian Shield: Devolatilization processes across the greenschist-amphibolite facies transition. In *Metamorphic Geology: Microscale to Mountain Belts*; Ferrero, S., Lanari, P., Goncalves, P., Grosch, E.G., Eds.; The Geological Society of London: London, UK, 2018; Volume 478, pp. 287–313.
23. Hamimi, Z.; Fowler, A.R. Najd Shear System in the Arabian-Nubian Shield. In *The Geology of the Arabian-Nubian Shield. Regional Geology Reviews*; Hamimi, Z., Fowler, A.R., Liégeois, J.P., Collins, A., Abdelsalam, M.G., Abd EI-Wahed, M., Eds.; Springer: Cham, Switzerland, 2021; pp. 359–392.
24. Stern, R.J.; Ali, K. Crustal Evolution of the Egyptian Precambrian Rocks. In *The Geology of Egypt, Regional Geology Reviews*; Springer: Cham, Switzerland, 2020; pp. 153–189.
25. Helmy, H.M.; Kaindl, R.; Fritz, H.; Loizenbauer, J. The Sukari gold mine, eastern Desert-Egypt: Structural setting, mineralogy and fluid inclusion study. *Miner. Depos.* **2004**, *39*, 495–511. [CrossRef]
26. Zoheir, B.A. Transpressional zones in ophiolitic mélange terranes: Potential exploration targets for gold in the South Eastern Desert, Egypt. *J. Geochem. Explor.* **2011**, *111*, 23–38. [CrossRef]
27. Zoheir, B.A. Lode-gold mineralization in convergent wrench structures: Examples from South Eastern Desert, Egypt. *J. Geochem. Explor.* **2012**, *114*, 82–97. [CrossRef]
28. Zoheir, B.A. Controls on lode gold mineralization, Romite deposit, South Eastern Desert, Egypt. *Geosci. Front.* **2012**, *3*, 571–585. [CrossRef]
29. Emam, A.; Zoheir, B. Au and Cr mobilization through metasomatism: Microchemical evidence from ore-bearing listvenite, South Eastern Desert of Egypt. *J. Geochem. Explor.* **2013**, *125*, 34–45. [CrossRef]
30. Rosenqvist, A.; Shimada, M.; Watanabe, M.; Tadono, T.; Yamauchi, K. Implementation of systematic data observation strategies for ALOS PALSAR, PRISM andAVNIR-2. In Proceedings of the 2004 IEEE International Geoscience and Remote Sensing Symposium, Anchorage, AK, USA, 20–24 September 2004.

31. Paillou, P.; Lopez, S.; Farr, T.; Rosenqvist, A. Mapping subsurface geology in Sahara using L-Band SAR: First results from the ALOS/PALSAR imaging Radar. *IEEE J. Sel. Top. Appl. Earth Obs. Remote Sens.* **2010**, *3*, 632–636. [CrossRef]
32. Abrams, M.; Tsu, H.; Hulley, G.; Iwao, K.; Pieri, D.; Cudahy, T.; Kargel, J. The Advanced Spaceborne Thermal Emission and Reflection Radiometer (ASTER) after Fifteen Years: Review of Global Products. *Int. J. Appl. Earth Obs. Geoinf.* **2015**, *38*, 292–301. [CrossRef]
33. Paek, S.W.; Balasubramanian, S.; Kim, S.; de Weck, O. Small-Satellite Synthetic Aperture Radar for Continuous Global Biospheric Monitoring: A Review. *Remote Sens.* **2020**, *12*, 2546. [CrossRef]
34. Abdelsalam, M.G.; Robinson, C.; El-Baz, F.; Stern, R. Application of orbital imaging radar for geologic studies in arid regions: The Saharan Testimony. *Photogramm. Eng. Remote Sens.* **2000**, *66*, 717–726.
35. Kusky, T.M.; Ramadan, T.M. Structural controls on Neoproterozoic mineralization in the South Eastern Desert, Egypt: An integrated field, Landsat TM, and SIR-C/X SAR approach. *J. Afr. Earth Sci.* **2002**, *35*, 107–121. [CrossRef]
36. Pour, A.B.; Hashim, M.; Makoundi, C.; Zaw, K. Structural Mapping of the Bentong-Raub Suture Zone Using PALSAR Remote Sensing Data, Peninsular Malaysia: Implications for Sedimenthosted/Orogenic Gold Mineral Systems Exploration. *Resour. Geol.* **2016**, *66*, 368–385. [CrossRef]
37. Pour, A.B.; Park, T.S.; Park, Y.; Hong, J.K.; Zoheir, B.; Pradhan, B.; Ayoobi, I.; Hashim, M. Application of multi-sensor satellite data for exploration of Zn-Pb sulfide mineralization in the Franklinian Basin, North Greenland. *Remote Sens.* **2018**, *10*, 1186. [CrossRef]
38. Pour, B.A.; Hashim, M. Structural mapping using PALSAR data in the Central Gold Belt, Peninsular Malaysia. *Ore Geol. Rev.* **2015**, *64*, 13–22. [CrossRef]
39. Hunt, G.R. Spectral Signatures of Particulate Minerals in the Visible and Near Infrared. *Geophysics* **1997**, *42*, 501–513. [CrossRef]
40. Clark, R.N.; King, T.V.V.; Klejwa, M.; Swayze, G.A.; Vergo, N. High spectral resolution reflectance spectroscopy of minerals. *J. Geophys. Res.* **1990**, *95*, 12653–12680. [CrossRef]
41. El Ramly, M.F.; Hussein, A.A. *The Alkaline Ring Complex of Egypt*; Paper No. 63; Egypt Geological Survey: Cairo, Egypt, 1983.
42. Sadek, M.F.; Tolba, M.I.; Yousef, M.M.; Abdel Gawad, G.M.; Salem, S.M.; Atia, S.A. *Geology of Wadi Kreiga-Gabal Korbiai Area, South Eastern Desert, Egypt*; Report of Expedition 9/95; Egypt Geological Survey: Cairo, Egypt, 1996.
43. Tolba, M.I. Geological and Petrological Studies on the Basement Complex in the Area around Bir Madi, South Eastern Desert, Egypt. Ph.D. Thesis, Ain Shams University, Cairo, Egypt, 2000; p. 247.
44. Egyptian Geological Survey and Mining Authority (EGSMA). *Geological Map of Marsa Shaab Quadrangle, Egypt*; Scale.1: 250,000; Egyptian Geological Survey and Mining Authority (EGSMA): Cairo, Egypt, 2002.
45. Stern, R.J.; Kroner, A.; Manton, W.I.; Reischmann, T.; Mansour, M.; Hussein, I.M. Geochronology of the Late Precambrian Hamisana shear zone, Red Sea Hills, Sudan and Egypt. *J. Geol. Soc. Lond.* **1989**, *146*, 1017–1029. [CrossRef]
46. Miller, M.M.; Dixon, T.H. Late Proterozoic evolution of the northern part of the Hamisana zone, northeast Sudan: Constraints on Pan-African accretionary tectonics. *J. Geol. Soc. Lond.* **1992**, *149*, 743–750. [CrossRef]
47. Abdel-Karim, A.M.; Soliman, M.M.; El-Kazzaz, Y.A.; Mazhar, A.A.; Abdel-Gawad, G.M. Geological and geochemical characteristics of the mafic–ultramafic rocks of Gabal Gerf Area, Southeastern Desert of Egypt. *Ann. Geol. Surv. Egypt* **2001**, *24*, 193–218.
48. Gahlan, H.A. Petrological Characteristics of the Mantle Section in the Proterozoic Ophiolites from the Pan-African Belt. Ph.D. Thesis, Kanazawa University, Kanazawa, Japan, 2006; p. 227.
49. De Wall, H.; Greiling, R.O.; Sadek, M.F. Post-collisional shortening in the late Pan-African Hamisana high strain zone, SE Egypt: Field and magnetic fabric evidence. *Precambrian Res.* **2001**, *107*, 179–194. [CrossRef]
50. Ali-Bik, M.W.; Sadek, M.F.; Ghabria, L.D.S. Late Neoproterozoic metamorphic assemblages along the Pan-African Hamisana Shear Zone, southeastern Egypt: Metamorphism, geochemistry and petrogenesis. *J. Afr. Earth Sci.* **2014**, *99*, 24–38. [CrossRef]
51. Bennet, J.D.; Mosley, P.N. Tiered-tectonics and evolution, Eastern Desert and Sinai, Egypt. In Proceedings of the 14th Colloquium on African Geology, Berlin, Germany, 18 August 1987; pp. 79–82.
52. Greiling, R.O.; Abdeen, M.M.; Dardir, A.A.; El Akhal, H.; El Ramly, M.F.; Kamal, G.E.D.; Sadek, M.F. A structural synthesis of the Proterozoic Arabian-Nubian Shield in Egypt. *Geol. Rundsch.* **1994**, *83*, 484–501. [CrossRef]
53. Zimmer, M.; Kröner, A.; Jochum, K.P.; Reischmann, T.; Todt, W. The Gabal Gerf complex: A Precambrian N-MORB ophiolite in the Nubian Shield, NE Africa. *Chem. Geol.* **1995**, *123*, 29–51. [CrossRef]
54. Abdel-Karim, A.M.; Ahmed, Z. Possible origin of the ophiolites of Eastern Desert, Egypt, from geochemical perspectives. *Arab. J. Sci. Eng.* **2010**, *35*, 115–143.
55. Sadek, M.F. Geology and spectral characterization of the basement rocks at Gabal Gerf area, Southeastern Egypt, Egypt. *J. Remote Sens. Space Sci.* **2005**, *8*, 109–128.
56. Sadek, M.F.; Ali-Bik, M.W.; Hassan, S.M. Late Neoproterozoic basement rocks of Kadabora-Suwayqat area, Central Eastern Desert, Egypt: Geochemical and remote sensing characterization. *Arab. J. Geosci.* **2015**, *8*, 10459–10479. [CrossRef]
57. Hassan, S.; Sadek, M. Geological mapping and spectral based classification of basement rocks using remote sensing data analysis: The Korbiai-Gerf nappe complex, South Eastern Desert. *Egypt. J. Asian Earth Sci.* **2017**, *134*, 404–418. [CrossRef]
58. Kröner, A.; Todt, W.; Hussein, I.M.; Mansour, M.; Rashwan, A.A. Dating of late Proterozoic ophiolites in Egypt and the Sudan using the single grain zircon evaporation technique. *Precambrian Res.* **1992**, *59*, 15–32. [CrossRef]

59. Ali, K.A.; Azer, M.K.; Gahlan, H.A.; Wilde, S.A.; Samuel, M.D.; Stern, R.J. Age constraints on the formation and emplacement of Neoproterozoic ophiolites along the Allaqi–Heiani Suture, South Eastern Desert of Egypt. *Gondwana Res.* **2010**, *18*, 583–595. [CrossRef]
60. Van der Meer, F.; Van der Werff, H.M.A.; Van Ruitenbeek, F.J.A. Potential of ESA's Sentinel-2 for geological applications. *Remote Sens. Environ.* **2014**, *148*, 124–133. [CrossRef]
61. Attema, E.; Bargellini, P.; Edwards, P.; Levrini, G.; Lokas, S.; Moeller, L.; Rosich-Tell, B.; Secchi, P.; Torres, R.; Davidson, M. Sentinel-1: The Radar Mission for GMES Operational Land and Sea Services. *ESA Bull.* **2007**, *131*, 10–17.
62. Balzter, H.; Cole, B.; Thiel, C.; Schmullius, C. Mapping CORINE Land Cover from Sentinel-1A SAR and SRTM Digital Elevation Model Data using Random Forests. *Remote Sens.* **2015**, *7*, 14876–14898. [CrossRef]
63. Igarashi, T. ALOS Mission requirement and sensor specification. *Adv. Space Res.* **2001**, *28*, 127–131. [CrossRef]
64. Earth Remote Sensing Data Analysis Center (ERSDAC). *PALSAR User's Guide*, 1st ed.; ERSDAC, Technical Department II, PALSAR Data Service Section: Japan, 2019. Available online: http://www.eorc.jaxa.jp/ALOS/en/doc/alos_userhb_en.pdf (accessed on 3 September 2022).
65. Sheng, Y.; Xia, Z. A comprehensive evaluation of filters for radar speckle suppression. In Proceedings of the 1996 International Geoscience and Remote Sensing Symposium (IGARSS '96), Lincoln, NE, USA, 31 May 1996.
66. Ge, W.; Cheng, Q.; Tang, Y.; Jing, L.; Gao, C. Lithological classification using sentinel-2A data in the Shibanjing ophiolite complex in Inner Mongolia, China. *Remote Sens.* **2018**, *10*, 638. [CrossRef]
67. Khan, S.D.; Mahmood, K.; Casey, J.F. Mapping of Muslim Bagh ophiolite complex (Pakistan) using new remote sensing, and field data. *J. Asian Earth Sci.* **2007**, *30*, 333–343. [CrossRef]
68. Pournamdari, M.; Hashim, M.; Pour, A.B. Application of ASTER and Landsat TM Data for Geological Mapping of Esfandagheh Ophiolite Complex, Southern Iran. *Resour. Geol.* **2014**, *64*, 233–246. [CrossRef]
69. Green, A.A.; Berman, M.; Switzer, P.; Craig, M.D. A transformation for ordering multispectral data in terms of image quality with implications for noise removal. *IEEE Trans. Geosci. Remote Sens.* **1988**, *26*, 65–74. [CrossRef]
70. Gupta, R.P.; Tiwari, R.K.; Saini, V.; Srivastava, N.A. Simplified approach for interpreting principal component images. *Adv. Remote Sens.* **2013**, *2*, 111–119. [CrossRef]
71. Ninomiya, Y.; Fu, B.; Cudhy, T.J. Detecting lithology with Advanced Spaceborne Thermal Emission and Refection Radiometer (ASTER) multispectral thermal infrared "radiance-at-sensor" data. *Remote Sens. Environ.* **2005**, *99*, 127–135. [CrossRef]
72. Ding, C.; Liu, X.; Liu, W.; Liu, M.; Li, Y. Mafic-ultramafic and quartz-rich indices deduced from ASTER thermal infrared data using a linear approximation to the Planck function. *Ore Geol. Rev.* **2014**, *60*, 161–173. [CrossRef]
73. Crósta, A.P.; Souza Filho, C.R.; Azevedo, F.; Brodie, C. Targeting key alteration minerals in epithermal deposits in Patagonia, Argentina, using ASTER imagery and principal component analysis. *Int. J. Remote Sens.* **2003**, *24*, 4233–4240. [CrossRef]
74. Ninomiya, Y. A Stabilized Vegetation Index and Several Mineralogic Indices Defined for ASTER VNIR and SWIR Data. In Proceedings of the IEEE 2003 International Geosciences and Remote Sensing Symposium (IGARSS '03), Toulouse, France, 21–25 July 2003; pp. 1552–1554.
75. Harsanyi, J.C.; Farrand, W.; Chang, C.I. Detection of subpixel spectral signatures in hyperspectral image sequences. In Proceedings of the American Society for Photogrammetry and Remote Sensing, Phoenix, AZ, USA, 25–27 October 1994; pp. 236–247.
76. Eldosouky, A.M.; Pour, A.; Hamed, A.; Taha, A.; Gamal, M.; Mahmoud, A.; Pham, L. Utilization of Landsat-8 Imagery and Aeromagnetic Data for Deciphering Alteration Zones and Structures: Implications for Mineral Exploration in the Southeastern Desert of Egypt. *FSRT J.* **2021**, *2*, 19–28. [CrossRef]
77. El Naggar, A.A.; Ahmad, A.A.; Salama, F.M.; Moselhy, N.A.; Ali, A.B.; Awad, S.M.; Oweiss, K.A. *Geological and Geochemical Exploration at North Gabal Gerf Area, South Eastern Desert, Egypt*; Expedition No. 12/2001; Egypt Geological Survey: Cairo, Egypt, 2002; pp. 1–107.
78. El Shimi, K.; Hassan, A.A.; Ali, M.; El Miligy, A.B. *Report on Reconnaissance Survey of Ancient Gold Occurrences at Southeastern Corner of Eastern Desert, Egypt*; Expedition No. G6/2010; Egypt Geological Survey: Cairo, Egypt, 2012; pp. 1–40.
79. Mars, J.C.; Rowan, L.C. *Mapping Phyllic and Argillic-Altered Rocks in Southeastern Afghanistan Using Advanced Spaceborne Thermal Emission and Reflection Radiometer (ASTER) Data*; Open-File Report 2007-1006; USGS: Denver, CO, USA, 2007.
80. Bannari, A.; El-Battay, A.; Saquaque, A.; Miri, A. PALSAR-FBS L-HH Mode and Landsat-TM Data Fusion for Geological Mapping. *Adv. Remote Sens.* **2016**, *5*, 246–268. [CrossRef]
81. Lang, F.; Yang, J.; Li, D. Adaptive-window polarimetric SAR image speckle filtering based on a homogeneity measurement. *IEEE Trans. Geosci. Remote Sens.* **2015**, *53*, 5435–5446. [CrossRef]
82. Klemm, D.; Klemm, R.; Murr, A. Gold of the Pharaohs-6000 years of gold mining in Egypt and Nubian. *J. Afr. Earth Sci.* **2001**, *33*, 643–659. [CrossRef]
83. McClay, K.; Bonora, M. Analog models of restraining stepovers in strike-slip fault systems. *Am. Assoc. Petrol. Geol.* **2001**, *85*, 233–260.
84. Sedki, T. Placer Gold Deposits in Madari Gold Mine, Southern Eastern Desert, Egypt: Orientation, Source and Distribution. *World Acad. Sci. Eng. Technol. Int. J. Geol. Environ. Eng.* **2021**, *15*, 18–24.
85. Said, A.; Zaghlol, K.; El Shimi, K. Gold bearing-quartz veins in island arc metavolcanics, case study: Wadi mahasin, west Qusier, Central Eastern Desert, Egypt. *Ann. Geol. Surv. Egypt* **2015**, *32*, 177–188.

86. Hassan, O.A.; El-Manakhly, M.M. Gold deposits in the southern Eastern Desert, Egypt. In *A Commodity Package*; Egyptian Geological Survey and Mining Authority: Cairo, Egypt, 1986.
87. Zoheir, B.A.; Emam, A. Field and ASTER imagery data for the setting of gold mineralization in Western Allaqi–Heiani belt, Egypt: A case study from the Haimur deposit. *J. Afr. Earth Sci.* **2014**, *99*, 150–164. [CrossRef]
88. Abu El-Leil, A.; Soliman, N.M.A.; Bekiet, M.H.; Elhebiry, M.A. Enhancing multispectral remote sensing data interpretation for historical gold mines in Egypt: A case study from Madari gold mine. *Arab. J. Geosci.* **2019**, *12*, 3. [CrossRef]
89. Oweiss, K.A.; Shabaan, G.M.; El-Shamy, M.H.; Abdel-Razik, K.A.; Khattab, M.M. *Report on Detailed Geological and Geochemical Exploration at Gabal Gerf Area, South Eastern Desert, Egypt*; Internal Report No. 47/96; Egypt Geological Survey: Cairo, Egypt, 1996.
90. Malczewski, J. GIS-Based Multicriteria Decision Analysis: A Survey of the Literature. *Int. J. Geogr. Inf. Sci.* **2006**, *20*, 703–726. [CrossRef]
91. Shebl, A.; Csamer, A. Stacked vector multi-source lithologic classification utilizing Machine Learning Algorithms: Data potentiality and dimensionality monitoring. *Remote Sens. Appl. Soc. Environ.* **2021**, *24*, 100643. [CrossRef]
92. Shebl, A.; Kusky, T.; Csamer, A. Advanced land imager superiority in lithological classification utilizing machine learning algorithms. *Arab. J. Geosci.* **2022**, *15*, 923. [CrossRef]
93. Shebl, A.; Csamer, A. Reappraisal of DEMs, Radar and optical datasets in lineaments extraction with emphasis on the spatial context. *Remote Sens. Appl. Soc. Environ.* **2021**, *24*, 100617. [CrossRef]
94. Mohamed, M.T.A.; Al-Naimi, L.S.; Mgbeojedo, T.I.; Agoha, C.C. Geological mapping and mineral prospectivity using remote sensing and GIS in parts of Hamissana, Northeast Sudan. *J. Pet. Explor. Prod. Technol.* **2021**, *11*, 1123–1138. [CrossRef]
95. Taha, M.A.M.; Xi, Y.; He, Q.; Hu, A.; Wang, S.; Liu, X. Investigating the Capabilities of Various Multispectral Remote Sensors Data to Map Mineral Prospectivity Based on Random Forest Predictive Model: A Case Study for Gold Deposits in Hamissana Area, NE Sudan. *Minerals* **2022**, *13*, 49. [CrossRef]
96. Abdelkareem, M.; Al-Arifi, N. Synergy of Remote Sensing Data for Exploring Hydrothermal Mineral Resources Using GIS-Based Fuzzy Logic Approach. *Remote Sens.* **2021**, *13*, 4492. [CrossRef]
97. Abd El-Wahed, M.A.; Attia, M. Structural and tectonic evolution of suture-related belts and post-accretionary systems in the Arabian-Nubian Shield. *Geol. J.* **2023**. [CrossRef]